UHASSELT

Upscaling a Navier-Stokes-Cahn-Hilliard model for two-phase porous-media flow with solute-dependent surface tension effects

S. Sharmin, M. Bastidas, C. Bringedal, I.S. Pop

Upscaling a Navier-Stokes-Cahn-Hilliard model for two-phase porous-media flow with solute-dependent surface tension effects

S. Sharmin[a], M. Bastidas[a,b,c], C. Bringedal[d] and I. S. Pop[a]

[a]Faculty of Sciences, Hasselt University, Diepenbeek, Belgium; [b] Inria, 2 rue Simone Iff, 75589 París, Francia; [c] CERMICS, Ecole des Ponts, 77455 Marne-la-Vallée, Francia; [d] Stuttgart Center for Simulation Science, Institute for Modelling Hydraulic and Environmental Systems, University of Stuttgart, Stuttgart, Germany

ABSTRACT
We consider a model for the flow of two immiscible and incompressible fluid phases in a porous medium. A surfactant is dissolved in one of the fluid phases, and its concentration at the interface separating the two fluids can change the surface tension. At the scale of pores, we assume that the flow is governed by the Navier-Stokes equations, while for the phase separation a Cahn-Hilliard phase-field model is adopted. Using formal homogenization, we derive a two-scale model describing the averaged behaviour of the system at the larger Darcy scale, where effective quantities are found through local (cell) problems at the smaller pore scale. For this two-scale model, we formulate a numerical scheme and present numerical results highlighting the influence of the solute-dependent surface tension.

1. Introduction

Many real-life applications of societal and technological relevance involve two-phase flow in porous media. Examples in this sense are groundwater remediation, or oil recovery from reservoirs. In such situations, the flow and transport processes take place at the scale of pores, which is here considered the micro scale. Moreover, in enhanced oil recovery [1,2], or applications involving e.g. microfluidics [3,4], or thin-film flows [5,6], the surface tension between the two fluid phases is influenced by a solute present in one or both fluids.

Since the porous medium consists of many pores and its geometry is highly complex, numerical simulations using mathematical models defined at the pore scale would not be feasible for practical purposes. Moreover, in most cases the primary interest is in the averaged behaviour of the system at a much larger scale, namely the scale of the application. This scale will be named from now one the Darcy scale, and can be viewed as a macro scale in contrast to the pore scale. From this prospect, it would be sufficient to use Darcy-scale models in the numerical simulation. However, when doing

so, it becomes difficult to account properly for the processes at the pore scale. The main challenges are finding the appropriate equations, parameters at the Darcy scale and incorporating the pore-scale effects.

The starting point here is a pore-scale model, where two fluids occupy two disjoint subdomains of the pore space. The fluids are assumed incompressible and immiscible, and are separated by an interface that moves with the fluids, thus in an a-priori unknown manner. Furthermore, a (soluble) surfactant species is present in one of the fluid phases. Its concentration affects the surface tension and, consequently, it influences the evolution of the fluid-fluid interface. As follows from the above, the pore-scale model is involving a free boundary, and is defined in a complex domain, namely the pore space of a porous medium. It includes two major components: the flow of the two separate phases, and the diffusion and transport of the soluble surfactant.

When dealing with free-boundary problems, one can consider several mathematical modelling strategies. The simplest situation is when the domain is either one-dimensional, or has a simple, rectangular or cylindrical structure, and the free boundary is along the symmetry axis. In this case, one can identify the free boundary through the distance to the domain boundary parts that are along the symmetry axis. Such a strategy is adopted e.g. in [7,8]. In a similar context, but with a free boundary that is transversal to the symmetry axis, parametric curves or surfaces have been used to model two-phase flow in a pore [9,10].

More realistic situations can be considered when assuming periodically distributed grains. In this case, the simplest approach is to assume a radial symmetry for the grain, as well as for the free boundary. Then, the free boundary can be identified through the radius of the curve/surface, as done e.g. in [11,12], where a model for water diffusion into absorbent particles is proposed. If the radial symmetry cannot be assumed, level sets can be used to identify the free boundary (see, e.g., [13–16]).

In the approaches mentioned above, the main difficulty in the analysis and numerical simulation of such mathematical models is related to the free boundary. To avoid using free boundaries and, consequently, working with time-dependent domains, the phase-field approach offers a good alternative. In this case, the free boundary is approximated by a diffuse interface region, and the model is hence defined in a fixed domain [17,18]. The phase-field indicator is a smooth approximation of, say, the characteristic function of the domain occupied by one of the fluid phases. Then, a critical aspect is to guarantee that, whenever the diffuse interface parameter approaches 0, the model reduces to the original one, involving free boundaries. Phase-field models can capture topological changes such as merging and splitting, and have thus been used successfully for direct numerical simulation of multi-phase flows [19,20]. For different applications we refer to [21,22], where a (pore-scale) phase-field model is developed for a precipitation-dissolution model involving one fluid phase, to [23,24] for two fluid phases, to [25] for two-phase flow including a temperature-dependent surface tension, and to [26,27] for fracture propagation in porelastic media.

In this paper, we derive a two-scale model for the two-phase flow in a porous medium, in which surfactant-dependent surface-tension effects are taken into account. More specifically, at the pore scale, the surface tension depends on the concentration of the surfactant, which is soluble in one of the fluid phases. The starting point is a Cahn-Hiliard [28] approximation of the phase separation together with the Navier-Stokes equations for the flow of the two fluids. Such models have been considered in [29–31]. Alternatively, in [32–34] the pore-scale flow is described by the Stokes model. We prefer to use the Navier-stokes equation for capturing fully the physics of the two-phase fluid flow at the pore scale. We highlight that a thermodynamically consistent

phase-field model for two-phase flow was first derived in [29], and later, two-phase flow models with surfactants were considered in [30]. Our model builds upon the model B derived in [30], where two-phase flow with variable surface tension is considered and the phase-field approach within a free energy framework is used to model the phase separation. We consider the instantaneous adsorption regime in [30], and simplify the model by assuming that the surfactant is only present in one of the fluid phases. Concerning numerical methods for similar type of models as discussed here, we refer to [35], where energy-stable schemes are proposed for a Cahn-Hiliard model for two-phase flow and surfactant transport, and to [36,37], where energy-stable methods based on discontinuous Galerkin discretization are analyzed.

Referring strictly to two-phase flow in porous media, various upscaling techniques can be considered to derive Darcy-scale models. In this sense, we mention simple transversal averaging, volume averaging, and homogenization techniques. The former can be applied when a simple geometry is assumed, as done e.g. in [7–10,38]. For volume averaging we refer to [31,39,40]. For rigorous homogenization we refer to [41–43], where the convergence of the upscaling process is proved.

Here we employ homogenization techniques for the formal derivation of the two-scale two-phase flow model, accounting for the surface-tension effects, as depending on the surfactant dissolved in one fluid phase. More precisely, we use formal asymptotic expansion methods and assume local periodicity at the pore scale. For similar results, we refer to [33,34,44,45] where no surfactant is present in the model, and to [32], where a solute transport component is included in the model, but without affecting the surface tension.

This paper is organized as follows. In Section 2, we present the Cahn-Hillard-Navier-Stokes two-phase flow model with solute-dependent surface tension and give the sharp-interface limit of the phase-field model. In Section 3, we derive the upscaled model from the non-dimensional pore-scale phase-field model using the asymptotic expansion method. In Section 4, we present the numerical scheme for solving the two-scale model and then solve this model for some test cases in Section 5. Finally, in Section 6, we draw our conclusions and give some remarks for future research.

2. The pore-scale model

Here we discuss the pore-scale model for the two-phase flow in a porous medium. The fluids are assumed incompressible and immiscible. For each fluid phase, the flow is governed by the Navier-Stokes model, defined in the corresponding sub-domain, and with fluid-specific parameters. The model accounts for a concentration-dependent surface tension. The surfactant is assumed soluble in one of the two fluid phases, and its concentration solves a convection-diffusion equation defined in the sub-domain of the solvent.

The fluid-fluid interface appears as free boundaries at the pore scale. To describe its movement, one considers the force balance of stress connected to the surface tension and the tangential stress force. The surface tension varies with the surfactant concentration at the separating interface.

As mentioned before, to overcome the difficulties related to the free boundaries, we use the phase-field approximation developed in [30], in which one works with a mixture of both fluids. However, by excepting a thin diffuse interface region, one can identify sub-domains in which one or another fluid is predominant. The evolution of the phase field is given by the Cahn-Hilliard equation.

In what follows, we let Ω denote the entire the pore space. Its boundary, $\partial\Omega$, has two parts: an inner one, the pore walls, and an outer one, the boundary of the entire medium. We consider the time interval $[0,\infty)$, and let $Q = [0,\infty) \times \Omega$.

2.1. The phase-field model

In the phase-field model, the interface separating the two immiscible fluids is approximated by a diffuse interface. A phase indicator $\phi : Q \to \mathbb{R}$ accounts for the presence of the two fluids, taking values either close to 1 in points occupied mainly by fluid 1 or close to -1 in points occupied mainly by fluid 2. We let $\rho, \mu, \boldsymbol{v}$ denote the density, viscosity and velocity of the mixture. Observe that these depend on ϕ. Following [29,30] the energy of the fluid-fluid interface is approximated by the Ginzburg-Landau energy functional

$$e_{\text{free}}(\phi, \nabla\phi) = \mathcal{C}\left(\frac{1}{\lambda}P(\phi) + \frac{\lambda}{2}|\nabla\phi|^2\right),\tag{1}$$

where $\lambda > 0$ is the thickness of the diffuse interfacial region, $\mathcal{C} = \frac{3}{2\sqrt{2}}$ is a calibration constant, while $P : \mathbb{R} \to \mathbb{R}$ is the double-well potential defined as

$$P(\phi) = \frac{1}{4}(1-\phi^2)^2.\tag{2}$$

2.1.1. The Cahn-Hilliard equations

We use the convective Cahn-Hilliard equation

$$\partial_t\phi + \nabla\cdot(\boldsymbol{v}\phi) = m\,\lambda\,\Delta\psi,\text{ in }Q,\tag{3a}$$

to describe the phase separation. Here, the Cahn-Hilliard mobility $m > 0$ is assumed constant. Different choices for mobility are given in [29], leading to various sharp-interface models in the limit $\lambda \to 0$.

We let c denote the concentration of the solute present in fluid 1 and $\gamma(c)$ the concentration-dependent surface tension. We assume that γ is linearly decreasing, namely the Henry isotherm (see [30])

$$\gamma(c) = \gamma_0 - B\,\beta\,c.\tag{3b}$$

Here γ_0 is the surface tension of a clean interface, B is the sensitivity of the surface tension to the surfactant, and $\beta > 0$ is a constant which is connected to the length scale. Following Model B in [30], which corresponds to instantaneous adsorption, and considering (3b), we use the potential ψ given by

$$\psi = -\nabla\cdot(\mathcal{C}\lambda\gamma(c)\nabla\phi) + \frac{\mathcal{C}}{\lambda}\gamma(c)P'(\phi) + \frac{1}{\beta}\gamma(c)I'(\phi),\text{ in }Q,\tag{3c}$$

where $I : \mathbb{R} \to \mathbb{R}$ is defined as

$$I(\phi) = \frac{1}{2}(1+\phi).\tag{3d}$$

As shown in [30], when $\lambda \to 0$, the phase field ϕ approaches the sign graph and therefore $I(\phi)$ approaches the characteristic function of fluid 1. Note the last term in (3c), which is added to include the effect of the varying surface tension.

For simplicity, we assume homogeneous Neumann boundary conditions for the phase field ϕ, as well as for the chemical potential ψ

$$\nabla \phi \cdot \boldsymbol{n} = 0, \text{ and } \nabla \psi \cdot \boldsymbol{n} = 0, \text{ on } \partial \Omega, \text{ for } t > 0, \tag{3e}$$

where $\boldsymbol{n}$ is the unit normal to $\partial \Omega$ pointing out of Ω. The first boundary condition corresponds to a 90° contact angle, and the second is needed for conserving the mass of the phase field.

The Cahn-Hilliard equations (3a), (3c) are completed by the initial condition

$$\phi(0, \cdot) = \phi_{\text{int}}, \text{ in } \Omega, \tag{3f}$$

where $\phi_{\text{int}} : \Omega \to \mathbb{R}$ is a given function approximating the initial distribution of the two fluids in Ω.

2.1.2. The flow equations

Since the mixture velocity is volume averaged, and since we assume there is no excess volume after mixing, $\boldsymbol{v}$ is divergence free (see [29]),

$$\nabla \cdot \boldsymbol{v} = 0, \text{ in } Q. \tag{3g}$$

For $\mathtt{i} = 1, 2$, we let $\rho^{(\mathtt{i})}$ and $\mu^{(\mathtt{i})}$ be the (constant) mass densities and (constant) viscosities of fluid $\mathtt{i}$. Here, the density and viscosity of the mixture are defined as $\rho(\phi) = \frac{\rho^{(1)} \cdot (1+\phi)}{2} + \frac{\rho^{(2)} \cdot (1-\phi)}{2}, \quad \mu(\phi) = \frac{\mu^{(1)} \cdot (1+\phi)}{2} + \frac{\mu^{(2)} \cdot (1-\phi)}{2}$.

The momentum conservation law is a modified Navier-Stokes equation

$$\begin{aligned} &\partial_t \left(\rho(\phi) \boldsymbol{v} \right) + \nabla \cdot \left(\rho(\phi) \boldsymbol{v} \otimes \boldsymbol{v} \right) - \nabla \cdot \left(-p \boldsymbol{I} + 2\mu(\phi)\varepsilon(\boldsymbol{v}) + \boldsymbol{v} \otimes \rho'(\phi) \lambda \, m \, \nabla \psi \right) \\ &= \nabla \cdot \left(\gamma(c) \left(e_{\text{free}}(\phi, \nabla \phi) \boldsymbol{I} - \mathcal{C} \lambda \nabla \phi \otimes \nabla \phi \right) \right), \text{ in } Q, \end{aligned} \tag{3h}$$

where $\varepsilon(\boldsymbol{v}) := \frac{1}{2} \left((\nabla \boldsymbol{v}) + (\nabla \boldsymbol{v})^T \right)$ is the symmetric stress tensor and p is a rescaled pressure. Here the flux term $(\boldsymbol{v} \otimes \rho'(\phi) \lambda \, m \, \nabla \psi)$ ensures thermodynamic consistency (see [29] and [30] for details) and the last two terms in (3h) account for the surface tension between the fluids. While such effects can be included in various ways (see [46]), here we adopt the approach in [30], based on the energy term $e_{\text{free}}(\phi, \nabla \phi) \boldsymbol{I}$ appearing in (3h). For convenience, from now on we use the following equivalent formulation of the momentum equation (3h)

$$\begin{aligned} &\partial_t \left(\rho(\phi) \boldsymbol{v} \right) + \nabla \cdot \left(\rho(\phi) \boldsymbol{v} \otimes \boldsymbol{v} \right) - \nabla \cdot \left(-p \boldsymbol{I} + 2\mu(\phi)\varepsilon(\boldsymbol{v}) + \boldsymbol{v} \otimes \rho'(\phi) \lambda \, m \, \nabla \psi \right) \\ &= \left(\frac{\mathcal{C}}{\lambda} \gamma(c) P'(\phi) - \nabla \cdot (\mathcal{C} \lambda \gamma(c) \nabla \phi) \right) \nabla \phi + \left(\frac{\mathcal{C}\lambda}{2} |\nabla \phi|^2 + \frac{\mathcal{C}}{\lambda} P(\phi) \right) \nabla \gamma(c), \text{ in } Q. \end{aligned} \tag{3i}$$

With $D > 0$ denoting the diffusion coefficient, the solute transport model reads

$$\partial_t (I(\phi)c) + \nabla \cdot (I(\phi)\boldsymbol{v}c) = \nabla \cdot (D \, I(\phi) \nabla c), \text{ in } Q. \tag{3j}$$

Note that as ϕ approaches -1, $I(\phi)$ vanishes, which is in line with the assumption that the solute is only present in fluid 1.

We assume that the velocity and solute flux are zero on the boundary

$$\boldsymbol{v} = \boldsymbol{0} \text{ and } I(\phi)\nabla c \cdot \boldsymbol{n} = 0 \text{ on } \partial\Omega, \text{ for } t > 0. \tag{3k}$$

Furthermore, the initial velocity and concentration are assumed known, $\boldsymbol{v}|_{t=0} = \boldsymbol{v}_{\text{int}}$ and $c|_{t=0} = c_{\text{int}}$ in Ω.

2.2. The sharp-interface limit of the phase-field model equations

Employing matched asymptotic methods, in [30] it is shown that, in the limit $\lambda \to 0$, the phase field model discussed above reduces to a sharp-interface model that will be given below. In this case, one has different quantities for each fluid phase, namely $\boldsymbol{v}^{(\mathtt{i})}, p^{(\mathtt{i})}$ ($\mathtt{i} = 1, 2$) standing for the velocity and pressure of fluid $\mathtt{i}$. Moreover, these quantities are defined in time-dependent subdomains $\Omega^{(\mathtt{i})}(t)$. More precisely, the sharp-interface model for fluid $\mathtt{i}$ reads

$$\partial_t \left(\rho^{(\mathtt{i})} \boldsymbol{v}^{(\mathtt{i})} \right) + \nabla \cdot \left(\rho^{(\mathtt{i})} \boldsymbol{v}^{(\mathtt{i})} \otimes \boldsymbol{v}^{(\mathtt{i})} \right) - \nabla \cdot \left(-p^{(\mathtt{i})} \boldsymbol{I} + 2\mu^{(\mathtt{i})} \varepsilon(\boldsymbol{v}^{(\mathtt{i})}) \right) = 0, \tag{4a}$$

$$\nabla \cdot \boldsymbol{v}^{(\mathtt{i})} = 0. \tag{4b}$$

for $t > 0$ and $\boldsymbol{x} \in \Omega^{\mathtt{i}}(t)$.

For the surfactant concentration, soluble only in fluid 1, we have

$$\partial_t c + \nabla \cdot \left(\boldsymbol{v}^{(1)} c \right) = \nabla \cdot (D\nabla c), \quad \text{in } \Omega^{(1)}(t), \text{ for } t > 0. \tag{4c}$$

The fluid-fluid interface $\Gamma(t)$ is a free boundary whose evolution is determined by the fluid velocities and the surface tension. For any $t > 0$, at $\Gamma(t)$, one has

$$\left[\boldsymbol{v}^{(\mathtt{i})} \right] = 0, \tag{4d}$$

$$\boldsymbol{v}^{(\mathtt{i})} \cdot \boldsymbol{n} = v_n, \tag{4e}$$

$$\left[-p^{(\mathtt{i})} \boldsymbol{I} + 2\mu^{(\mathtt{i})} \varepsilon(\boldsymbol{v}^{(\mathtt{i})}) \right] \boldsymbol{n} = \gamma(c)\kappa\boldsymbol{n} - \nabla_t\gamma(c), \tag{4f}$$

$$\left(-D\nabla c + \boldsymbol{v}^{(1)} c \right) \cdot \boldsymbol{n} = v_n\, c. \tag{4g}$$

Here $[.]$ stands for the jump of the quantities from $\Omega^{(1)}(t)$ to $\Omega^{(2)}(t)$, κ is the mean curvature of $\Gamma(t)$ and v_n its normal velocity. Moreover, $\nabla_t\gamma(c) := \nabla\gamma(c) - \boldsymbol{n}\,(\boldsymbol{n} \cdot \nabla\gamma(c))$ is the tangential stress gradient, where $\boldsymbol{n}$ is the unit normal vector on $\Gamma(t)$ pointing into $\Omega^{(1)}(t)$ from $\Omega^{(2)}(t)$.

3. Upscaling the pore-scale model to the Darcy scale

As stated in the introduction, we assume that, at the pore scale, the porous medium Ω consists of small but many periodically distributed impermeable grains, surrounded by a void space (the pore space). We are interested in the averaged behavior of the system, observed at the larger (Darcy) scale. At the same time, smaller (pore) scale

6

information should not be disregarded. The pore scale and the Darcy scale are assumed well separated. With ℓ and L being the characteristic lengths of the pore scale and of the Darcy scale, we use $\epsilon = \frac{\ell}{L} \ll 1$ as the scale separation parameter.

To define the pore-scale domain, we write $Y = [0, \ell]^d, (d = 2, 3)$ as the union of the grain $\mathcal{G}$, its boundary $\partial\mathcal{G}$ and the surrounding pore space $\mathcal{P}$,

$$Y = \mathcal{P} \cup \mathcal{G} \cup \partial\mathcal{G}.$$

The entire porous medium occupies the domain

$$\Omega = \cup_{w \in W_\Omega} \left\{ \ell \left(w + Y \right) \right\},$$

where $W_\Omega \subset \mathbb{Z}^d$ is a set of multi-indices. We assume that W_Ω is such that Ω is a connected set.

The phase-field model is defined in the entire pore space,

$$\Omega_\mathcal{P}^\epsilon = \cup_{w \in W_\Omega} \left\{ \ell \left(w + \mathcal{P} \right) \right\},$$

which is also assumed to be connected.

The boundary of $\Omega_\mathcal{P}^\epsilon$ consists of the outer part, $\partial\Omega$, and the inner part, which is the union of the grain boundaries,

$$\Gamma_\mathcal{G}^\epsilon = \cup_{w \in W_\Omega} \left\{ \ell \left(w + \partial\mathcal{G} \right) \right\}.$$

Note that the grains are not part of $\Omega_\mathcal{P}^\epsilon$. See Figure 1 for a sketch of the domain.
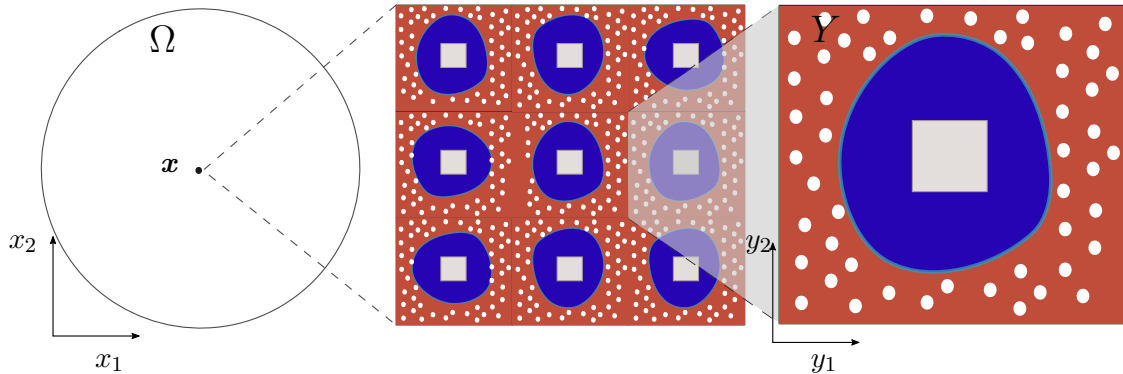

Figure 1. Schematic representation of the porous medium Ω. The figure in the middle presents periodically repeating grains (coloured gray) surrounded by void space (the pores) occupied by two immiscible fluids (blue and red). A surfactant soluble in fluid 1 is present (white particles). The right figure is a typical representation of a pore.

3.1. Non-dimensional model equations

For deriving the Darcy-scale model, we first bring the pore-scale model to a dimensionless form. To do so, we use the reference values and the non-dimensional quantities

7

in Table 1, and the non-dimensional numbers

$$\text{Eu} = \frac{p_{\text{ref}}}{\rho_{\text{ref}}v_{\text{ref}}^2}, \quad \text{Re} = \frac{\rho_{\text{ref}}v_{\text{ref}}x_{\text{ref}}}{\mu_{\text{ref}}}, \quad \text{Ca} = \frac{\mu_{\text{ref}}v_{\text{ref}}}{\gamma_{\text{ref}}},$$

$$\text{Pe}_c = \frac{v_{\text{ref}}x_{\text{ref}}}{D}, \quad \text{A}_\phi = \frac{m\psi_{\text{ref}}}{v_{\text{ref}}}, \quad \text{A}_\psi = \frac{\gamma_{\text{ref}}}{x_{\text{ref}}\psi_{\text{ref}}}. \tag{5}$$

Table 1. Reference values and non-dimensional quantities

Variables and parameters	Reference values	Units	Non-dimensional quantities
Time	t_{ref}	[s]	$\hat{t} = t/t_{\text{ref}}$
Space (Darcy scale)	$x_{\text{ref}} = L$	[m]	$\hat{\boldsymbol{x}} = \boldsymbol{x}/x_{\text{ref}}$
Space (pore scale)	$y_{\text{ref}} = \ell$	[m]	$\hat{\boldsymbol{y}} = \boldsymbol{y}/y_{\text{ref}}$
Velocity	$v_{\text{ref}} = x_{\text{ref}}/t_{\text{ref}}$	$[\frac{m}{s}]$	$\hat{\boldsymbol{v}} = \boldsymbol{v}/v_{\text{ref}}$
Pressure	p_{ref}	$[\frac{\text{kg}}{\text{m s}^2}]$	$\hat{p} = p/p_{\text{ref}}$
Molar concentration	c_{ref}	$[\frac{\text{mol}}{\text{m}^3}]$	$\hat{c} = c/c_{\text{ref}}$
Density	ρ_{ref}	$[\frac{\text{kg}}{\text{m}^3}]$	$\hat{\rho} = \rho/\rho_{\text{ref}}$
Viscosity	μ_{ref}	$[\frac{\text{kg}}{\text{m s}}]$	$\hat{\mu} = \mu/\mu_{\text{ref}}$
Surface tension	γ_{ref}	$[\frac{\text{kg}}{\text{s}^2}]$	$\hat{\gamma}(\hat{c}) = \gamma(c_{\text{ref}}\,\hat{c})/\gamma_{\text{ref}}$
Diffuse interface thickness	$\lambda_{\text{ref}} = y_{\text{ref}} = \ell$	[m]	$\hat{\lambda} = \lambda/y_{\text{ref}}$
	$\beta_{\text{ref}} = y_{\text{ref}} = \ell$	[m]	$\hat{\beta} = \beta/y_{\text{ref}}$
Free energy	$e_{\text{free,ref}} = \frac{1}{x_{\text{ref}}}$	$[\frac{1}{m}]$	$\hat{e}_{\text{free}} = e_{\text{free}}\, x_{\text{ref}}$
Cahn-Hilliard chemical potential	ψ_{ref}	$[\frac{\text{kg}}{\text{m s}^2}]$	$\hat{\psi} = \psi/\psi_{\text{ref}}$
Diffusion coefficient	D	$[\frac{\text{m}^2}{\text{s}}]$	
Cahn-Hilliard mobility	m	$[\frac{\text{m}^2\,\text{s}}{\text{kg}}]$	

Observe that the diffuse interface parameters λ and β are assumed to have the order of the pore-scale length ℓ. In dimensionless form, these are chosen of order $\mathcal{O}(\epsilon)$, but smaller than ϵ. Using the reference values and non-dimensional quantities from Table 1, and the non-dimensional numbers in (5), we obtain the dimensionless model

$$\partial_{\hat{t}}\left(\hat{\rho}(\phi)\hat{\boldsymbol{v}}\right) + \hat{\nabla}\cdot\left(\hat{\rho}(\phi)\hat{\boldsymbol{v}}\otimes\hat{\boldsymbol{v}}\right) = \hat{\nabla}\cdot\left(-\text{Eu}\,\hat{p}\boldsymbol{I} + \frac{1}{\text{Re}}2\hat{\mu}(\phi)\varepsilon(\hat{\boldsymbol{v}})\right)$$

$$+ \hat{\nabla}\cdot\left(\epsilon\text{A}_\phi\hat{\lambda}\hat{\rho}'(\phi)\hat{\boldsymbol{v}}\otimes\hat{\nabla}\hat{\psi}\right) + \frac{1}{\text{Re Ca}}\left(\frac{\mathcal{C}}{\epsilon\hat{\lambda}}\hat{\gamma}(\hat{c})P'(\phi) - \hat{\nabla}\cdot\left(\epsilon\mathcal{C}\hat{\lambda}\hat{\gamma}(\hat{c})\hat{\nabla}\phi\right)\right)\hat{\nabla}\phi$$

$$+ \frac{1}{\text{Re Ca}}\left(\frac{\epsilon\mathcal{C}\hat{\lambda}}{2}|\hat{\nabla}\phi|^2 + \frac{\mathcal{C}}{\epsilon\hat{\lambda}}P(\phi)\right)\hat{\nabla}\hat{\gamma}(\hat{c}), \tag{6a}$$

$$\hat{\nabla}\cdot\hat{\boldsymbol{v}} = 0, \tag{6b}$$

$$\partial_{\hat{t}}(I(\phi)\hat{c}) + \hat{\nabla}\cdot(I(\phi)\hat{\boldsymbol{v}}\hat{c}) = \frac{1}{\text{Pe}_c}\hat{\nabla}\cdot\left(I(\phi)\hat{\nabla}\hat{c}\right), \tag{6c}$$

$$\partial_{\hat{t}}\phi + \hat{\nabla}\cdot(\hat{\boldsymbol{v}}\phi) = \epsilon\text{A}_\phi\hat{\lambda}\hat{\Delta}\hat{\psi}, \tag{6d}$$

$$\hat{\psi} = \text{A}_\psi\left(\frac{\mathcal{C}}{\epsilon\hat{\lambda}}\hat{\gamma}(\hat{c})P'(\phi) + \frac{1}{\epsilon\hat{\beta}}\hat{\gamma}(\hat{c})I'(\phi) - \hat{\nabla}\cdot\left(\epsilon\mathcal{C}\hat{\lambda}\hat{\gamma}(\hat{c})\hat{\nabla}\phi\right)\right), \tag{6e}$$

for all $\boldsymbol{x} \in \hat{\Omega}_{\mathcal{P}}^{\epsilon}$ and $t > 0$. At the inner boundary $\hat{\Gamma}_{\mathcal{G}}^{\epsilon}$ and for $t > 0$, one has

$$\hat{\boldsymbol{v}} = 0, \tag{6f}$$

$$I(\phi)\hat{\nabla}\hat{c} \cdot \boldsymbol{n} = 0, \tag{6g}$$

$$\hat{\nabla}\phi \cdot \boldsymbol{n} = 0, \tag{6h}$$

$$\hat{\nabla}\hat{\psi} \cdot \boldsymbol{n} = 0. \tag{6i}$$

For the ease of presentation, since from now on only the non-dimensional quantities are considered, the hat is ommited in all notations.

3.2. Derivation of the two-scale model

We derive the upscaled counterpart of the phase-field model in Section 2.1. To do so, we employ formal asymptotic expansions w.r.t. ϵ. More precisely, we assume that all variables can be expanded regularly in terms of ϵ. For example, for ϕ one has

$$\phi(t, \boldsymbol{x}) = \phi_0(t, \boldsymbol{x}, \frac{\boldsymbol{x}}{\epsilon}) + \epsilon\phi_1(t, \boldsymbol{x}, \frac{\boldsymbol{x}}{\epsilon}) + \mathcal{O}(\epsilon^2), \tag{7}$$

where the functions ϕ_i are Y-periodic w.r.t. the last argument. In other words, for $\mathsf{j} = 1, \ldots, \mathsf{d}$ and with $\mathbf{e}_{\mathsf{j}}$ being the unit vector in the j-th direction, one has $\phi_i(t, \boldsymbol{x}, \boldsymbol{y} + \mathbf{e}_{\mathsf{j}}) = \phi_i(t, \boldsymbol{x}, \boldsymbol{y})$. Similar expansions are used for $p, \boldsymbol{v}, c$. Note that the spatial variable $\boldsymbol{x}$ is doubled into the slow one, $\boldsymbol{x}$, accounting for the changes at the Darcy scale, and the fast variable $\boldsymbol{y} = \frac{\boldsymbol{x}}{\epsilon}$, where the rapid oscillations occur. With this the j-th spatial derivative $\partial_{x_{\mathsf{j}}}$ becomes $\partial_{x_{\mathsf{j}}} + \frac{1}{\epsilon}\partial_{y_{\mathsf{j}}}$ and

$$\nabla = \frac{1}{\epsilon}\nabla_{\boldsymbol{y}} + \nabla_{\boldsymbol{x}}. \tag{8}$$

Observe that, unlike [45], we do not consider an additional fast time scale, and do not disregard the $O(\epsilon)$ terms in the expansion of the phase field and of the velocity. At this point, we assume the following scaling of the dimensionless numbers (5),

$$\begin{aligned}
\mathrm{Eu} &= \epsilon^{-2}\,\overline{\mathrm{Eu}}, \quad \mathrm{Re} = \overline{\mathrm{Re}}, \quad \mathrm{Ca} = \overline{\mathrm{Ca}}, \\
\mathrm{Pe}_c &= \overline{\mathrm{Pe}_c}, \qquad \mathrm{A}_\phi = \overline{\mathrm{A}_\phi}, \quad \mathrm{A}_\psi = \epsilon\overline{\mathrm{A}_\psi},
\end{aligned} \tag{9}$$

where $\overline{\mathrm{Eu}}, \overline{\mathrm{Re}}, \overline{\mathrm{Ca}}, \overline{\mathrm{Pe}_c}, \overline{\mathrm{A}_\phi}$ and $\overline{\mathrm{A}_\psi}$ do not depend on ϵ. By choosing this scaling of the Euler number Eu and of the Reynolds number Re, we make sure that we are in the regime where Darcy's law is applicable, which corresponds to a laminar flow driven by the pressure gradient. The scaling of the capillary number Ca is chosen moderate w.r.t. ϵ. This choice results in equal pressures in both phases. Further, the Péclet number Pe_c is of order 1, which corresponds to the time scales of solute transport by advection and diffusion being of the same order. For simplicity, here $\overline{\mathrm{Ca}} = \overline{\mathrm{Pe}_c} = 1$. The scaling of A_ϕ and A_ψ is needed for the phase-field interface dynamics to be active at the pore scale.

For the ease of presentation, the dependency of $t, \boldsymbol{x}$ and $\boldsymbol{y}$ will in the following only be written whenever needed. Also, recall that all model variables are Y-periodic.

3.2.1. The flow equations

Inserting the asymptotic expansions in the reformulated momentum and mass conservation equations (6a) and (6b), and in the no-slip boundary condition (6f), and applying (8), one obtains for all $t > 0$

$$-\frac{1}{\epsilon^3}\overline{\mathrm{Eu}}\nabla_{\boldsymbol{y}}p_0 - \frac{1}{\epsilon^2}\overline{\mathrm{Eu}}\left(\nabla_{\boldsymbol{x}}p_0 + \nabla_{\boldsymbol{y}}p_1\right) + \frac{1}{\epsilon^2}\frac{1}{\mathrm{Re}}\nabla_{\boldsymbol{y}}\cdot\left(2\mu(\phi_0)\varepsilon_{\boldsymbol{y}}(\boldsymbol{v}_0)\right)$$

$$+\frac{1}{\mathrm{Re\,Ca}}\frac{1}{\epsilon^2}\left\{\left(\frac{\mathcal{C}}{\lambda}\gamma(c_0)P'(\phi_0) - \mathcal{C}\lambda\nabla_{\boldsymbol{y}}\cdot\left(\gamma(c_0)\nabla_{\boldsymbol{y}}\phi_0\right)\right)\nabla_{\boldsymbol{y}}\phi_0\right.$$

$$\left.+\mathcal{C}\left(\frac{\lambda}{2}|\nabla_{\boldsymbol{y}}\phi_0|^2 + \frac{1}{\lambda}P(\phi_0)\right)\nabla_{\boldsymbol{y}}\gamma(c_0)\right\} + \mathcal{O}(\epsilon^{-1}) = 0, \qquad \text{in } \Omega \times \mathcal{P}, \quad (10\mathrm{a})$$

$$\frac{1}{\epsilon}\nabla_{\boldsymbol{y}}\cdot\boldsymbol{v}_0 + \nabla_{\boldsymbol{x}}\cdot\boldsymbol{v}_0 + \nabla_{\boldsymbol{y}}\cdot\boldsymbol{v}_1 + \mathcal{O}(\epsilon) = 0, \qquad \text{in } \Omega \times \mathcal{P}, \quad (10\mathrm{b})$$

$$\boldsymbol{v}_0 + \epsilon\boldsymbol{v}_1 + \mathcal{O}(\epsilon^2) = 0, \qquad \text{on } \Omega \times \partial\mathcal{G}. \quad (10\mathrm{c})$$

Since $|Y| = 1$, for all $t > 0$ and $\boldsymbol{x} \in \Omega$ we define the averaged velocity as

$$\bar{\boldsymbol{v}}(t, \boldsymbol{x}) := \int_{\mathcal{P}} \boldsymbol{v}_0(t, \boldsymbol{x}, \boldsymbol{y})\, d\boldsymbol{y}. \qquad (11)$$

The lowest order term in (10b) provides

$$\nabla_{\boldsymbol{y}}\cdot\boldsymbol{v}_0 = 0, \qquad (12)$$

for all $\boldsymbol{y} \in \mathcal{P}$. Next, the ϵ^0-order terms give

$$\nabla_{\boldsymbol{x}}\cdot\boldsymbol{v}_0 + \nabla_{\boldsymbol{y}}\cdot\boldsymbol{v}_1 = 0, \qquad (13)$$

for all $\boldsymbol{y} \in \mathcal{P}$. Integrating the above w.r.t $\boldsymbol{y}$, applying the Gauss theorem, and using the periodicity of $\boldsymbol{v}_1$ and the boundary condition $\boldsymbol{v}_1 = 0$ on $\partial\mathcal{G}$, one gets

$$\nabla_{\boldsymbol{x}}\cdot\bar{\boldsymbol{v}} = 0, \qquad (14)$$

for all $t > 0$ and $\boldsymbol{x} \in \Omega$. Equating the dominating $\mathcal{O}(\epsilon^{-3})$ term in (10a) gives

$$\nabla_{\boldsymbol{y}}p_0 = 0,$$

for all $\boldsymbol{y} \in \mathcal{P}$, so $p_0 = p_0(t, \boldsymbol{x})$. Further, in section 3.2.3 we also show that $c_0 = c_0(t, \boldsymbol{x})$ is independent of $\boldsymbol{y}$, and therefore, the last $\mathcal{O}(\epsilon^{-2})$ terms in (10a) are vanishing. Hence, the $\mathcal{O}(\epsilon^{-2})$ terms in (10a) yield

$$\overline{\mathrm{Eu}}\nabla_{\boldsymbol{y}}p_1 - \frac{1}{\overline{\mathrm{Re}}}\nabla_{\boldsymbol{y}}\cdot\left(2\mu(\phi_0)\varepsilon_{\boldsymbol{y}}(\boldsymbol{v}_0)\right) = -\overline{\mathrm{Eu}}\nabla_{\boldsymbol{x}}p_0$$

$$+\frac{1}{\overline{\mathrm{ReCa}}}\gamma(c_0)\left(\frac{\mathcal{C}}{\lambda}P'(\phi_0) - \mathcal{C}\lambda\Delta_{\boldsymbol{y}}\phi_0\right)\nabla_{\boldsymbol{y}}\phi_0, \qquad (15)$$

for all $t > 0$, $\boldsymbol{x} \in \Omega$ and $\boldsymbol{y} \in \mathcal{P}$.

Observe that (15) and (12) form a Stokes system in terms of the unknowns p_1 and $\boldsymbol{v}_0$, depending on p_0, ϕ_0 and c_0. This dependence can be made more precise through

10

the cell problems, defined for all $\boldsymbol{x} \in \Omega$ and $t > 0$,

$$
\begin{cases}
\overline{\overline{\text{Eu}}} \left(\mathbf{e}_{\mathbf{j}} + \nabla_{\boldsymbol{y}} \Pi_{\mathbf{j}} \right) = -\dfrac{1}{\overline{\overline{\text{Re}}}} \nabla_{\boldsymbol{y}} \cdot \left(2\mu(\phi_0) \varepsilon_{\boldsymbol{y}}(\mathbf{w}_{\mathbf{j}}) \right), & \text{in } \mathcal{P}, \\
\nabla_{\boldsymbol{y}} \cdot \mathbf{w}_{\mathbf{j}} = 0, & \text{in } \mathcal{P}, \\
\mathbf{w}_{\mathbf{j}} = \mathbf{0}, & \text{on } \partial\mathcal{G}, \\
\Pi_{\mathbf{j}}, \mathbf{w}_{\mathbf{j}} \text{ are } Y\text{-periodic and } \displaystyle\int_{\mathcal{P}} \Pi_{\mathbf{j}} \, d\boldsymbol{y} = 0,
\end{cases}
\tag{16}
$$

for $\mathbf{j} = 1, \dots, \mathbf{d}$, and

$$
\begin{cases}
\overline{\overline{\text{Eu}}} \nabla_{\boldsymbol{y}} \Pi_0 = -\dfrac{1}{\overline{\overline{\text{Re}}}} \nabla_{\boldsymbol{y}} \cdot \left(2\mu(\phi_0) \varepsilon_{\boldsymbol{y}}(\mathbf{w}_0) \right) \\
\qquad\qquad + \dfrac{1}{\overline{\overline{\text{Re}}}\, \overline{\overline{\text{Ca}}}} \left(\dfrac{\mathcal{C}}{\lambda} P'(\phi_0) - \mathcal{C}\lambda\Delta_{\boldsymbol{y}}\phi_0 \right) \nabla_{\boldsymbol{y}}\phi_0, & \text{in } \mathcal{P}, \\
\nabla_{\boldsymbol{y}} \cdot \mathbf{w}_0 = 0, & \text{in } \mathcal{P}, \\
\mathbf{w}_0 = \mathbf{0}, & \text{on } \partial\mathcal{G}, \\
\Pi_0, \mathbf{w}_0 \text{ are } Y\text{-periodic and } \displaystyle\int_{\mathcal{P}} \Pi_0 \, d\boldsymbol{y} = 0.
\end{cases}
\tag{17}
$$

By linearity, having solved the cell problems above, one immediately gets $\boldsymbol{v}_0$ and p_1 as functions of p_0, c_0 and, implicitly, of ϕ_0

$$
\boldsymbol{v}_0(t, \boldsymbol{x}, \boldsymbol{y}) = -\sum_{\mathbf{j}=1}^{d} \mathbf{w}_{\mathbf{j}}(t, \boldsymbol{x}, \boldsymbol{y}) \, \partial_{x_{\mathbf{j}}} p_0(t, \boldsymbol{x}) - \mathbf{w}_0(t, \boldsymbol{x}, \boldsymbol{y}) \, \gamma(c_0(t, \boldsymbol{x})),
\tag{18}
$$

$$
p_1(t, \boldsymbol{x}, \boldsymbol{y}) = \tilde{p}_1(t, \boldsymbol{x}) + \sum_{\mathbf{j}=1}^{d} \Pi_{\mathbf{j}}(t, \boldsymbol{x}, \boldsymbol{y}) \, \partial_{x_{\mathbf{j}}} p_0(t, \boldsymbol{x}) + \Pi_0(t, \boldsymbol{x}, \boldsymbol{y}) \gamma(c_0(t, \boldsymbol{x})).
\tag{19}
$$

Here $\tilde{p}_1 = \tilde{p}_1(t, \boldsymbol{x})$ is an arbitrary function not depending on $\boldsymbol{y}$. Integrating (18) w.r.t. $\boldsymbol{y}$ over $\mathcal{P}$ and using (11) yields

$$
\bar{\boldsymbol{v}} = -\mathcal{K}\nabla_{\boldsymbol{x}} p_0 - \boldsymbol{M}\gamma(c_0),
\tag{20}
$$

for all $\boldsymbol{x} \in \Omega$ and $t > 0$. The elements of the effective matrix $\mathcal{K}(t, \boldsymbol{x})$ and the components of the effective vector $\boldsymbol{M}(t, \boldsymbol{x})$ are obtained using the solutions of the cell problems (16) and (17),

$$
\mathcal{K}_{\mathbf{i},\mathbf{j}} = \int_{\mathcal{P}} \mathbf{w}_{\mathbf{i},\mathbf{j}} \, d\boldsymbol{y} \quad \text{and} \quad \boldsymbol{M}_{\mathbf{i}} = \int_{\mathcal{P}} \mathbf{w}_{\mathbf{i},0} \, d\boldsymbol{y}, \text{ with } \mathbf{i}, \mathbf{j} = 1, \dots, \mathbf{d},
\tag{21}
$$

where $\mathbf{w}_{\mathbf{i},\alpha}$ is the $\mathbf{i}$-th component of $\mathbf{w}_\alpha$ ($\alpha \in \{0, \dots, \mathbf{d}\}$).

3.2.2. The Cahn-Hilliard equations

By Taylor expansions about ϕ_0 and c_0, we can write

$$
P(\phi) = P(\phi_0) + \epsilon\phi_1 P'(\phi_0) + \mathcal{O}(\epsilon^2), \quad \gamma(c) = \gamma(c_0) + \epsilon c_1 \gamma'(c_0) + \mathcal{O}(\epsilon^2).
\tag{22}
$$

11

Using this and the homogenization ansatz (7) in equation (6d), (6e), (6h) and (6i), one gets for all $t > 0$

$$\mathcal{O}(\epsilon) = \frac{1}{\epsilon} \nabla_{\boldsymbol{y}} \cdot (\boldsymbol{v}_0 \phi_0) - \frac{1}{\epsilon} \overline{A_\phi} \lambda \Delta_{\boldsymbol{y}} \psi_0 + \partial_t \phi_0 + \nabla_{\boldsymbol{x}} \cdot (\boldsymbol{v}_0 \phi_0)$$
$$- \overline{A_\phi} \lambda \left(\nabla_{\boldsymbol{x}} \cdot (\nabla_{\boldsymbol{y}} \psi_0) + \nabla_{\boldsymbol{y}} \cdot (\nabla_{\boldsymbol{x}} \psi_0) + \Delta_{\boldsymbol{y}} \psi_1 \right), \qquad \text{in } \Omega \times \mathcal{P}, \qquad (23\text{a})$$

$$\mathcal{O}(\epsilon) = \psi_0 - \gamma(c_0) \overline{A_\psi} \left(\frac{\mathcal{C} P'(\phi_0)}{\lambda} + \frac{I'(\phi_0)}{\beta} - \mathcal{C} \lambda \Delta_{\boldsymbol{y}} \phi_0 \right), \qquad \text{in } \Omega \times \mathcal{P}, \qquad (23\text{b})$$

$$\mathcal{O}(\epsilon) = \frac{1}{\epsilon} \nabla_{\boldsymbol{y}} \phi_0 \cdot \boldsymbol{n} + \nabla_{\boldsymbol{x}} \phi_0 \cdot \boldsymbol{n} + \nabla_{\boldsymbol{y}} \phi_1 \cdot \boldsymbol{n}, \qquad \text{on } \Omega \times \partial \mathcal{G}, \qquad (23\text{c})$$

$$\mathcal{O}(\epsilon) = \frac{1}{\epsilon} \nabla_{\boldsymbol{y}} \psi_0 \cdot \boldsymbol{n} + \nabla_{\boldsymbol{x}} \psi_0 \cdot \boldsymbol{n} + \nabla_{\boldsymbol{y}} \psi_1 \cdot \boldsymbol{n}, \qquad \text{on } \Omega \times \partial \mathcal{G}. \qquad (23\text{d})$$

Since $|Y| = 1$, the porosity of the medium is defined as

$$\Phi := |\mathcal{P}|. \qquad (24)$$

We also define

$$\bar{\phi}(t, \boldsymbol{x}) := \frac{1}{\Phi} \int_{\mathcal{P}} \phi_0(t, \boldsymbol{x}, \boldsymbol{y}) \, d\boldsymbol{y}. \qquad (25)$$

Since ϕ_0 approaches 1 inside fluid 1, we use (3d) to define the fluid 1 saturation as

$$S := \frac{1}{\Phi} \int_{\mathcal{P}} I(\phi_0) d\boldsymbol{y} = \frac{1}{2} \left(1 + \bar{\phi} \right), \qquad (26)$$

for all $t > 0$ and $\boldsymbol{x} \in \Omega$. Equating the lowest order terms in (23a)-(23d), and using (26), one gets the local cell problem for the phase field and the potential,

$$\begin{cases} \nabla_{\boldsymbol{y}} \cdot (\boldsymbol{v}_0 \phi_0) = \overline{A_\phi} \lambda \Delta_{\boldsymbol{y}} \psi_0, & \text{in } \mathcal{P}, \\ \psi_0 = \gamma(c_0) \overline{A_\psi} \left(\frac{\mathcal{C} P'(\phi_0)}{\lambda} + \frac{I'(\phi_0)}{\beta} - \mathcal{C} \lambda \Delta_{\boldsymbol{y}} \phi_0 \right), & \text{in } \mathcal{P}, \\ \nabla_{\boldsymbol{y}} \phi_0 \cdot \boldsymbol{n} = 0, & \text{on } \partial \mathcal{G}, \qquad (27) \\ \nabla_{\boldsymbol{y}} \psi_0 \cdot \boldsymbol{n} = 0, & \text{on } \partial \mathcal{G}, \\ \phi_0, \psi_0 \text{ are } Y\text{-periodic, and } \frac{1}{\Phi} \int_{\mathcal{P}} \phi_0 \, d\boldsymbol{y} = 2 \, S - 1, \end{cases}$$

for all $t > 0$ and $\boldsymbol{x} \in \Omega$, where $\boldsymbol{v}_0$ is defined in (18). Observe that in the above equations only spatial derivatives w.r.t. $\boldsymbol{y}$ are present. The constraint $\frac{1}{\Phi} \int_{\mathcal{P}} \phi_0 \, d\boldsymbol{y} = 2 \, S - 1$ follows from (26) and ensures the uniqueness of a solution.

The ϵ^0-order terms in (23a) equate to

$$\partial_t \phi_0 + \nabla_{\boldsymbol{x}} \cdot (\boldsymbol{v}_0 \phi_0) = \overline{A_\phi} \lambda \left\{ \nabla_{\boldsymbol{x}} \cdot (\nabla_{\boldsymbol{y}} \psi_0) + \nabla_{\boldsymbol{y}} \cdot (\nabla_{\boldsymbol{x}} \psi_0) + \Delta_{\boldsymbol{y}} \psi_1 \right\}, \qquad (28)$$

for all $t > 0$, $\boldsymbol{x} \in \Omega$ and $\boldsymbol{y} \in \mathcal{P}$. Integrating the above equation over $\mathcal{P}$ w.r.t $\boldsymbol{y}$ and

using the periodicity of ψ_0 and ψ_1 yields

$$\partial_t \int_{\mathcal{P}} \phi_0 \, d\boldsymbol{y} + \nabla_{\boldsymbol{x}} \cdot \int_{\mathcal{P}} (\boldsymbol{v}_0 \phi_0) \, d\boldsymbol{y} = 0, \tag{29}$$

for all $t > 0$ and $\boldsymbol{x} \in \Omega$. Using (26), this becomes

$$\Phi \partial_t S + \frac{1}{2} \nabla_{\boldsymbol{x}} \cdot \bar{\boldsymbol{v}}^\phi = 0, \tag{30}$$

for all $t > 0$ and $\boldsymbol{x} \in \Omega$, where $\bar{\boldsymbol{v}}^\phi$ is the ϕ-dependent velocity given by

$$\bar{\boldsymbol{v}}^\phi(t, \boldsymbol{x}) := \int_{\mathcal{P}} \boldsymbol{v}_0(t, \boldsymbol{x}, \boldsymbol{y}) \phi_0(t, \boldsymbol{x}, \boldsymbol{y}) \, d\boldsymbol{y}. \tag{31}$$

Using (18) in the above equation, one finds

$$\bar{\boldsymbol{v}}^\phi = -\mathcal{K}^\phi \, \nabla_{\boldsymbol{x}} p_0 - \boldsymbol{M}^\phi \, \gamma(c_0), \tag{32}$$

for all $t > 0$ and $\boldsymbol{x} \in \Omega$, where the elements of the effective matrix $\mathcal{K}^\phi(t, \boldsymbol{x})$ and the components of the effective vector $\boldsymbol{M}^\phi(t, \boldsymbol{x})$ are defined by

$$\mathcal{K}^\phi_{\mathtt{i},\mathtt{j}} := \int_{\mathcal{P}} \mathbf{w}_{\mathtt{i},\mathtt{j}} \, \phi_0 \, d\boldsymbol{y} \quad \text{and} \quad \boldsymbol{M}^\phi_{\mathtt{i}} := \int_{\mathcal{P}} \mathbf{w}_{\mathtt{i},0} \, \phi_0 \, d\boldsymbol{y}, \text{ for } \mathtt{i}, \mathtt{j} = 1, \ldots, \mathtt{d}. \tag{33}$$

Again, $\mathbf{w}_{\mathtt{j}}$ and $\mathbf{w}_0$ are the solutions of the cell problems (16) and (17).

3.2.3. Solute conservation equation

Using the homogenization ansatz in (6c) and (6g) provides

$$-\frac{1}{\epsilon^2} \frac{1}{\mathrm{Pe}_c} \nabla_{\boldsymbol{y}} \cdot (I(\phi_0) \nabla_{\boldsymbol{y}} c_0) + \frac{1}{\epsilon} \nabla_{\boldsymbol{y}} \cdot (I(\phi_0) \boldsymbol{v}_0 c_0) - \frac{1}{\epsilon} \frac{1}{\mathrm{Pe}_c} \nabla_{\boldsymbol{x}} \cdot (I(\phi_0) \nabla_{\boldsymbol{y}} c_0)$$

$$-\frac{1}{\epsilon} \frac{1}{\mathrm{Pe}_c} \nabla_{\boldsymbol{y}} \cdot \left(I(\phi_0) \left(\nabla_{\boldsymbol{x}} c_0 + \nabla_{\boldsymbol{y}} c_1 \right) + \phi_1 \frac{1}{2} \nabla_{\boldsymbol{y}} c_0 \right) + \partial_t (I(\phi_0) c_0) + \nabla_{\boldsymbol{x}} \cdot (I(\phi_0) \boldsymbol{v}_0 c_0)$$

$$+ \nabla_{\boldsymbol{y}} \cdot \left(I(\phi_0) \left(\boldsymbol{v}_0 c_1 + \boldsymbol{v}_1 c_0 \right) + \phi_1 \frac{1}{2} \boldsymbol{v}_0 c_0 \right)$$

$$-\frac{1}{\overline{\mathrm{Pe}_c}} \nabla_{\boldsymbol{y}} \cdot \left(I(\phi_0) \left(\nabla_{\boldsymbol{x}} c_1 + \nabla_{\boldsymbol{y}} c_2 \right) + \phi_1 \frac{1}{2} \left(\nabla_{\boldsymbol{x}} c_0 + \nabla_{\boldsymbol{y}} c_1 \right) \right)$$

$$-\frac{1}{\overline{\mathrm{Pe}_c}} \nabla_{\boldsymbol{x}} \cdot \left(I(\phi_0) \left(\nabla_{\boldsymbol{x}} c_0 + \nabla_{\boldsymbol{y}} c_1 \right) + \phi_1 \frac{1}{2} \nabla_{\boldsymbol{y}} c_0 \right) + \mathcal{O}(\epsilon) = 0, \qquad \text{in } \Omega \times \mathcal{P}, \tag{34a}$$

$$\frac{1}{\epsilon} I(\phi_0) \nabla_{\boldsymbol{y}} c_0 \cdot \boldsymbol{n} + I(\phi_0) \left(\nabla_{\boldsymbol{x}} c_0 + \nabla_{\boldsymbol{y}} c_1 \right) \cdot \boldsymbol{n} + \epsilon I(\phi_0) \left(\nabla_{\boldsymbol{x}} c_1 + \nabla_{\boldsymbol{y}} c_2 \right) \cdot \boldsymbol{n}$$

$$+ \epsilon \phi_1 \frac{1}{2} \nabla_{\boldsymbol{y}} c_0 \cdot \boldsymbol{n} + \mathcal{O}(\epsilon^2) = 0, \qquad \text{on } \Omega \times \partial \mathcal{G}. \tag{34b}$$

The lowest order term from the above equations gives, for all $t > 0$ and $\boldsymbol{x} \in \Omega$,

$$\nabla_{\boldsymbol{y}} \cdot (I(\phi_0)\nabla_{\boldsymbol{y}} c_0) = 0, \quad \text{in } \mathcal{P}, \text{ and}$$
$$I(\phi_0)\nabla_{\boldsymbol{y}} c_0 \cdot \boldsymbol{n} = 0, \quad \text{on } \partial\mathcal{G}.$$

Using the Y-periodicity of c_0, one immediately gets that $c_0 = c_0(t, \boldsymbol{x})$ is independent of $\boldsymbol{y}$. Further, the ϵ^{-1}-order terms in (34a) equate to

$$\frac{1}{\overline{\text{Pe}_c}}\nabla_{\boldsymbol{y}} \cdot (I(\phi_0)\nabla_{\boldsymbol{y}} c_1) = -\frac{1}{\overline{\text{Pe}_c}}\nabla_{\boldsymbol{y}} \cdot (I(\phi_0)\nabla_{\boldsymbol{x}} c_0) + c_0 \left(\nabla_{\boldsymbol{y}} \cdot (I(\phi_0)\boldsymbol{v}_0)\right), \quad (35)$$

for all $t > 0$, $\boldsymbol{x} \in \Omega$ and $\boldsymbol{y} \in \mathcal{P}$. This, together with the boundary condition (34b), allows obtaining c_1 in terms of ϕ_0, c_0 and $\boldsymbol{v}_0$, by solving the cell problems

$$\begin{cases} \nabla_{\boldsymbol{y}} \cdot \left[I(\phi_0)\left(\nabla_{\boldsymbol{y}}\chi_{\mathsf{j}} + \mathbf{e}_{\mathsf{j}}\right)\right] = 0, & \text{in } \mathcal{P}, \\ I(\phi_0)\left(\nabla_{\boldsymbol{y}}\chi_{\mathsf{j}} + \mathbf{e}_{\mathsf{j}}\right) \cdot \boldsymbol{n} = 0, & \text{on } \partial\mathcal{G}, \\ \chi_{\mathsf{j}} \text{ is } Y\text{-periodic and } \int_{\mathcal{P}} \chi_{\mathsf{j}} \, d\boldsymbol{y} = 0, \end{cases} \quad (36)$$

for $\mathsf{j} = 1, \ldots, \mathsf{d}$, and

$$\begin{cases} \nabla_{\boldsymbol{y}} \cdot \left[I(\phi_0)\nabla_{\boldsymbol{y}}\chi_0\right] = \nabla_{\boldsymbol{y}} \cdot (I(\phi_0)\boldsymbol{v}_0), & \text{in } \mathcal{P}, \\ I(\phi_0)\nabla_{\boldsymbol{y}}\chi_0 \cdot \boldsymbol{n} = 0, & \text{on } \partial\mathcal{G}, \\ \chi_0 \text{ is } Y\text{-periodic and } \int_{\mathcal{P}} \chi_0 \, d\boldsymbol{y} = 0. \end{cases} \quad (37)$$

With (36) and (37), one has for all $t > 0$, $\boldsymbol{x} \in \Omega$ and $\boldsymbol{y} \in \mathcal{P}$

$$c_1(t, \boldsymbol{x}, \boldsymbol{y}) = \tilde{c}_1(t, \boldsymbol{x}) + \sum_{\mathsf{j}=1}^{d} \chi_{\mathsf{j}}(t, \boldsymbol{x}, \boldsymbol{y}) \, \partial_{x_{\mathsf{j}}} c_0(t, \boldsymbol{x}) + \chi_0(t, \boldsymbol{x}, \boldsymbol{y})c_0(t, \boldsymbol{x}), \quad (38)$$

where $\tilde{c}_1 = \tilde{c}_1(t, \boldsymbol{x})$ is arbitrary. Finally, the ϵ^0-order terms in (34a) equate to

$$\partial_t(I(\phi_0)c_0) + \nabla_{\boldsymbol{x}} \cdot (I(\phi_0)\boldsymbol{v}_0 c_0) - \frac{1}{\overline{\text{Pe}_c}}\nabla_{\boldsymbol{x}} \cdot (I(\phi_0)\left(\nabla_{\boldsymbol{x}} c_0 + \nabla_{\boldsymbol{y}} c_1\right))$$
$$= -\nabla_{\boldsymbol{y}} \cdot \left(I(\phi_0)\left(\boldsymbol{v}_0 c_1 + \boldsymbol{v}_1 c_0\right) + \phi_1 \frac{1}{2}\boldsymbol{v}_0 c_0\right) + \frac{1}{\overline{\text{Pe}_c}}\nabla_{\boldsymbol{y}} \cdot (I(\phi_0)\left(\nabla_{\boldsymbol{x}} c_1 + \nabla_{\boldsymbol{y}} c_2\right)) \quad (39)$$
$$+ \frac{1}{\overline{\text{Pe}_c}}\nabla_{\boldsymbol{y}} \cdot \left(\phi_1 \frac{1}{2}\left(\nabla_{\boldsymbol{x}} c_0 + \nabla_{\boldsymbol{y}} c_1\right)\right),$$

for all $t > 0$, $\boldsymbol{x} \in \Omega$ and $\boldsymbol{y} \in \mathcal{P}$. Integrating the above w.r.t $\boldsymbol{y}$ over $\mathcal{P}$, using the definitions of the averaged velocity and ϕ-dependent velocity in (11) and (31), together with the periodicity, one gets the macroscopic law for the solute conservation

$$\Phi \, \partial_t \left(S \, c_0\right) + \frac{1}{2}\nabla_{\boldsymbol{x}} \cdot \left(c_0 \left(\bar{\boldsymbol{v}} + \bar{\boldsymbol{v}}^{\phi}\right)\right) = \frac{1}{\overline{\text{Pe}_c}}\nabla_{\boldsymbol{x}} \cdot (\mathcal{B}\nabla_{\boldsymbol{x}} c_0 + \boldsymbol{H} c_0), \quad (40)$$

for all $t > 0$ and $\boldsymbol{x} \in \Omega$. Here the elements of the effective matrix $\mathcal{B}(t, \boldsymbol{x})$ and the components of the effective vector $\boldsymbol{H}(t, \boldsymbol{x})$ are determined by

$$\mathcal{B}_{\mathtt{i},\mathtt{j}} = \int_{\mathcal{P}} I(\phi_0) \left(\delta_{\mathtt{i}\mathtt{j}} + \partial_{\boldsymbol{y}_{\mathtt{i}}} \chi_{\mathtt{j}} \right) \, d\boldsymbol{y}, \quad \boldsymbol{H}_{\mathtt{i}} = \int_{\mathcal{P}} I(\phi_0) \partial_{\boldsymbol{y}_{\mathtt{i}}} \chi_0 \, d\boldsymbol{y}, \qquad (41)$$

for $\mathtt{i}, \mathtt{j} = 1, \ldots, \mathtt{d}$, and where $\chi_{\mathtt{j}}$ and χ_0 solve the cell problems (36) and (37).

3.3. Summary of upscaled model

To simplify the notation, from here we give up the indices 0 in $\boldsymbol{v}_0, \phi_0, \psi_0, p_0$, and c_0. With this, the Darcy-type laws in (20) and (32) for the velocities, and the mass conservation laws for the two fluids and for the solute in (14), (30), and (40) can be written as

$$\bar{\boldsymbol{v}} = -\mathcal{K} \, \nabla p - \boldsymbol{M} \, \gamma(c), \tag{42a}$$

$$\nabla \cdot \bar{\boldsymbol{v}} = 0, \tag{42b}$$

$$\Phi \, \partial_t S + \frac{1}{2} \nabla \cdot \bar{\boldsymbol{v}}^\phi = 0, \tag{42c}$$

$$\bar{\boldsymbol{v}}^\phi = -\mathcal{K}^\phi \, \nabla p - \boldsymbol{M}^\phi \, \gamma(c), \tag{42d}$$

$$\Phi \, \partial_t (S \, c) + \frac{1}{2} \nabla \cdot \left(c \left(\bar{\boldsymbol{v}} + \bar{\boldsymbol{v}}^\phi \right) \right) = \frac{1}{\mathrm{Pe}_c} \nabla \cdot (\mathcal{B} \, \nabla c + \boldsymbol{H} \, c), \tag{42e}$$

defined for all $t > 0$ and $\boldsymbol{x} \in \Omega$. The Darcy-scale unknowns are $\bar{\boldsymbol{v}}(t, \boldsymbol{x})$, $S(t, \boldsymbol{x})$, $\bar{\boldsymbol{v}}^\phi(t, \boldsymbol{x})$, $p(t, \boldsymbol{x})$, and $c(t, \boldsymbol{x})$. This system is completed with boundary conditions on $\partial \Omega$, and the initial solute concentration c_{int}. Moreover, an initial (pore-scale) phase field ϕ_{int} is prescribed at each Darcy-scale point, yielding an initial saturation S_{int} satisfying (26). The effective parameters $\mathcal{K}, \mathcal{K}^\phi, \boldsymbol{M}, \boldsymbol{M}^\phi, \mathcal{B}$ and $\boldsymbol{H}$ are obtained by solving cell problems, as given in Table 2.

Table 2. Parameters for the upscaled model (42).

Effective parameters	Cell problems
$\mathcal{K}_{\mathtt{i},\mathtt{j}} = \int_{\mathcal{P}} \mathbf{w}_{\mathtt{i},\mathtt{j}} \, d\boldsymbol{y}$, $\mathcal{K}_{\mathtt{i},\mathtt{j}}^\phi = \int_{\mathcal{P}} \mathbf{w}_{\mathtt{i},\mathtt{j}} \, \phi \, d\boldsymbol{y}$.	$\overline{\mathrm{Eu}} \, (\mathbf{e}_{\mathtt{j}} + \nabla_{\boldsymbol{y}} \Pi_{\mathtt{j}}) = -\frac{1}{\mathrm{Re}} \nabla_{\boldsymbol{y}} \cdot (2\mu(\phi) \varepsilon_{\boldsymbol{y}}(\mathbf{w}_{\mathtt{j}}))$, in $\mathcal{P}$, $\nabla_{\boldsymbol{y}} \cdot \mathbf{w}_{\mathtt{j}} = 0$, in $\mathcal{P}$, $\mathbf{w}_{\mathtt{j}} = \mathbf{0}$, on $\partial \mathcal{G}$, $\Pi_{\mathtt{j}}, \mathbf{w}_{\mathtt{j}}$ are Y-periodic and $\int_{\mathcal{P}} \Pi_{\mathtt{j}} \, d\boldsymbol{y} = 0$, for $\mathtt{j} = 1, \ldots \mathtt{d}$.
$\boldsymbol{M}_{\mathtt{i}} = \int_{\mathcal{P}} \mathbf{w}_{\mathtt{i},0} \, d\boldsymbol{y}$, $\boldsymbol{M}_{\mathtt{i}}^\phi = \int_{\mathcal{P}} \mathbf{w}_{\mathtt{i},0} \, \phi \, d\boldsymbol{y}$.	$\overline{\mathrm{Eu}} \nabla_{\boldsymbol{y}} \Pi_0 = -\frac{1}{\mathrm{Re}} \nabla_{\boldsymbol{y}} \cdot (2\mu(\phi) \varepsilon_{\boldsymbol{y}}(\mathbf{w}_0)) + \frac{1}{\mathrm{Re} \, \mathrm{Ca}} \left(\frac{\mathcal{C}}{\lambda} P'(\phi) - \mathcal{C} \lambda \Delta_{\boldsymbol{y}} \phi \right) \nabla_{\boldsymbol{y}} \phi$, in $\mathcal{P}$, $\nabla_{\boldsymbol{y}} \cdot \mathbf{w}_0 = 0$, in $\mathcal{P}$, $\mathbf{w}_0 = \mathbf{0}$, on $\partial \mathcal{G}$, $\Pi_0, \mathbf{w}_0$ are Y-periodic and $\int_{\mathcal{P}} \Pi_0 \, d\boldsymbol{y} = 0$.
$\mathcal{B}_{\mathtt{i},\mathtt{j}} = \int_{\mathcal{P}} I(\phi) \left(\delta_{\mathtt{i}\mathtt{j}} + \partial_{\boldsymbol{y}_{\mathtt{i}}} \chi_{\mathtt{j}} \right) \, d\boldsymbol{y}$.	$\nabla_{\boldsymbol{y}} \cdot [I(\phi) \left(\nabla_{\boldsymbol{y}} \chi_{\mathtt{j}} + \mathbf{e}_{\mathtt{j}} \right)] = 0$, in $\mathcal{P}$, $I(\phi) \left(\nabla_{\boldsymbol{y}} \chi_{\mathtt{j}} + \mathbf{e}_{\mathtt{j}} \right) \cdot \boldsymbol{n} = 0$, on $\partial \mathcal{G}$, $\chi_{\mathtt{j}}$ is Y-periodic and $\int_{\mathcal{P}} \chi_{\mathtt{j}} \, d\boldsymbol{y} = 0$, for $\mathtt{j} = 1, \ldots \mathtt{d}$.
$\boldsymbol{H}_{\mathtt{i}} = \int_{\mathcal{P}} I(\phi) \partial_{\boldsymbol{y}_{\mathtt{i}}} \chi_0 \, d\boldsymbol{y}$.	$\nabla_{\boldsymbol{y}} \cdot [I(\phi) \nabla_{\boldsymbol{y}} \chi_0] = \nabla_{\boldsymbol{y}} \cdot (I(\phi_0) \boldsymbol{v})$, in $\mathcal{P}$, $I(\phi) \nabla_{\boldsymbol{y}} \chi_0 \cdot \boldsymbol{n} = 0$, on $\partial \mathcal{G}$, χ_0 is Y-periodic and $\int_{\mathcal{P}} \chi_0 \, d\boldsymbol{y} = 0$.

To calculate the effective quantities, one needs the phase field $\phi(t, \boldsymbol{x}, \boldsymbol{y})$. This is

obtained by solving for all $t > 0$ and $\boldsymbol{x} \in \Omega$ the problem

$$
\begin{cases}
\nabla_{\boldsymbol{y}} \cdot (\boldsymbol{v}\phi) = \overline{\mathrm{A}_\phi} \lambda \Delta_{\boldsymbol{y}} \psi, & \text{in } \mathcal{P}, \\[2mm]
\psi = \overline{\mathrm{A}_\psi} \gamma(c) \left(\dfrac{\mathcal{C} P'(\phi)}{\lambda} + \dfrac{I'(\phi)}{\beta} - \mathcal{C} \lambda \Delta_{\boldsymbol{y}} \phi \right), & \text{in } \mathcal{P}, \\[2mm]
\nabla_{\boldsymbol{y}} \phi \cdot \boldsymbol{n} = 0, \nabla_{\boldsymbol{y}} \psi \cdot \boldsymbol{n} = 0 & \text{on } \partial \mathcal{G}, \\[2mm]
\phi \text{ and } \psi \text{ are } Y\text{-periodic and } \dfrac{1}{\Phi} \displaystyle\int_{\mathcal{P}} \phi \, d\boldsymbol{y} = 2\, S - 1.
\end{cases}
\tag{43}
$$

Here $\boldsymbol{v}$ is nothing but the pore-scale velocity $\boldsymbol{v}_0$ in (18), namely

$$
\boldsymbol{v}(t, \boldsymbol{x}, \boldsymbol{y}) = -\sum_{j=1}^{d} \mathbf{w}_j(t, \boldsymbol{x}, \boldsymbol{y}) \, \partial_{x_j} p(t, \boldsymbol{x}) - \mathbf{w}_0(t, \boldsymbol{x}, \boldsymbol{y}) \, \gamma(c(t, \boldsymbol{x})).
\tag{44}
$$

Remark 1. Inspired by the definition of the fluid 1 saturation S in (26), and since $\frac{1}{2} \left(\bar{\boldsymbol{v}} + \bar{\boldsymbol{v}}^\phi \right) = \frac{1}{2} \int_{\mathcal{P}} \boldsymbol{v}_0 (1 + \phi) \, d\boldsymbol{y}$ and $\frac{1}{2} \left(\bar{\boldsymbol{v}} - \bar{\boldsymbol{v}}^\phi \right) = \frac{1}{2} \int_{\mathcal{P}} \boldsymbol{v}_0 (1 - \phi) \, d\boldsymbol{y}$, one can identify the quantities corresponding to fluid i and reformulate the Darcy-scale equations accordingly. More precisely, we consider the (Darcy-scale) fluid-specific quantities

$$
\begin{aligned}
S^{(1)} &= S, & \bar{\boldsymbol{v}}^{(1)} &= \frac{1}{2} \left(\bar{\boldsymbol{v}} + \bar{\boldsymbol{v}}^\phi \right), & \mathcal{K}^{(1)} &= \frac{(\mathcal{K} + \mathcal{K}^\phi)}{2}, & \boldsymbol{M}^{(1)} &= \frac{(\boldsymbol{M} + \boldsymbol{M}^\phi)}{2}, \\[2mm]
S^{(2)} &= 1 - S, & \bar{\boldsymbol{v}}^{(2)} &= \frac{1}{2} \left(\bar{\boldsymbol{v}} - \bar{\boldsymbol{v}}^\phi \right), & \mathcal{K}^{(2)} &= \frac{(\mathcal{K} - \mathcal{K}^\phi)}{2}, & \boldsymbol{M}^{(2)} &= \frac{(\boldsymbol{M} - \boldsymbol{M}^\phi)}{2}.
\end{aligned}
$$

Then, for all $t > 0$ and $\boldsymbol{x} \in \Omega$, the Darcy-scale equations (42a)-(42d) become

$$
\bar{\boldsymbol{v}}^{(i)} = -\mathcal{K}^{(i)} \nabla p - \boldsymbol{M}^{(i)} \gamma(c),
\tag{45a}
$$

$$
\Phi \partial_t S^{(i)} + \nabla \cdot \bar{\boldsymbol{v}}^{(i)} = 0,
\tag{45b}
$$

Observe that (45a) and (45b) are similar to the standard effective model for two-phase flow, when assuming a zero capillary pressure, respectively that the phase pressures are equal. In simplifed geometries, such models are derived by transversal averaging, but assuming that the capillary number is moderate compared to ϵ, namely $O(1)$ (see [8,10]). Moreover, (45a) are enriched Darcy laws, where the last terms account for the surfactant effects, leading to a variable surface-tension. Additionally, $\mathcal{K}^{(i)}$ is the relative permeability of fluid i multiplied by the absolute permeability of the medium, and $\boldsymbol{M}^{(i)}$ is connected to the effective variable surface-tension effect of the fluid phases. Finally, since $\bar{\boldsymbol{v}}^{(1)} + \bar{\boldsymbol{v}}^{(2)} = \bar{\boldsymbol{v}}$, (42b) implies that the total flow is divergence free.

Models disregarding the capillary pressure effects are quite popular in the numerical simulation of two-phase porous-media flows. Compared to these, even if the presence of a soluble surfactant is disregarded, one aspect is much different in the Darcy-scale model derived here. Commonly used models build on a relationship between the relative permeability of a fluid phase and its saturation. Here, no such relationship is assumed, as the permeability is obtained from the pore scale, by solving the corresponding cell problems.

4. An explicit numerical scheme

For solving the two-scale model summarized in Section 3.3, we consider a simple, explicit numerical scheme. Given $N \in \mathbb{N}$, we define the time step $\Delta t := \mathrm{T}/N$ and let $t^n = n\Delta t$. The time-discrete functions are denoted by

$$\phi^n := \phi(t^n, \cdot, \cdot), \quad \nu^n := \nu(t^n, \cdot) \quad \text{and} \quad \eta_{\mathsf{j}}^n := \eta_{\mathsf{j}}(t^n, \cdot),$$

where $\nu \in \{\mathcal{K}^\phi, \mathcal{K}, \boldsymbol{M}^\phi, \boldsymbol{M}, \mathcal{B}, \boldsymbol{H}, p, \bar{\boldsymbol{v}}, \bar{\boldsymbol{v}}^\phi, S, c\}$, and $\eta_{\mathsf{j}} \in \{\Pi_{\mathsf{j}}, \mathbf{w}_{\mathsf{j}}, \chi_{\mathsf{j}}\}$ with $\mathsf{j} = 0, 1, \dots \mathsf{d}$. We denote the given initial data c^0, ϕ^0 and S^0, where S^0 satisfies (26). At each time step $n \geq 0$, the following steps are carried out.

Step 1. For each $\boldsymbol{x} \in \Omega$, compute the solution of the time-discrete counterpart of (16) and (17), i.e. obtain $(\Pi_{\mathsf{j}}^n, \mathbf{w}_{\mathsf{j}}^n)$ with $\mathsf{j} = 0, 1, \dots \mathsf{d}$.

Step 2. Compute the time-discrete effective parameters $\mathcal{K}^{\phi,n}$, $\mathcal{K}^n$, $\boldsymbol{M}^{\phi,n}$ and $\boldsymbol{M}^n$.

Step 3. Compute the solution of the time-discrete counterpart of (42a) and (42b). Specifically, obtain p^n and $\bar{\boldsymbol{v}}^n$ by solving

$$
\begin{aligned}
\bar{\boldsymbol{v}}^n &= -\mathcal{K}^n \nabla p^n - \boldsymbol{M}^n \gamma(c^n), \\
\nabla \cdot \bar{\boldsymbol{v}}^n &= 0.
\end{aligned}
\tag{46}
$$

Step 4. Use the explicit, time-discrete counterpart of (42c) and (42d) to compute

$$
\begin{aligned}
\bar{\boldsymbol{v}}^{\phi,n} &= -\mathcal{K}^{\phi,n} \nabla p^n - \boldsymbol{M}^{\phi,n} \gamma(c^n), \\
S^{n+1} &= S^n - \frac{\Delta t}{2\Phi} \nabla \cdot \bar{\boldsymbol{v}}^{\phi,n}.
\end{aligned}
\tag{47}
$$

Step 5. For each $\boldsymbol{x} \in \Omega$, compute the pore-scale velocity $\boldsymbol{v}^n$ as in (18). Solve the time-discrete counterpart of (36) and (37), i.e. obtain $\chi^{\mathsf{j},n}$ with $\mathsf{j} = 0, 1, \dots \mathsf{d}$.

Step 6. Compute the second set of time-discrete effective parameters $\mathcal{B}^n$ and $\boldsymbol{H}^n$.

Step 7. Compute the solution of the time-discrete counterpart of (42e). Specifically, obtain c^{n+1} by solving the following time-discrete problem

$$
S^{n+1} c^{n+1} = S^n c^n + \frac{\Delta t}{\mathrm{Pe}_c \, \Phi} \nabla \cdot \left(\mathcal{B}^n \nabla c^{n+1} \right) - \frac{\Delta t}{2 \, \Phi} \nabla \cdot \left[\left(\bar{\boldsymbol{v}}^n + \bar{\boldsymbol{v}}^{\phi,n} - \frac{1}{\mathrm{Pe}_c} \vec{H}^n \right) c^n \right]. \tag{48}
$$

Step 8. For each $\boldsymbol{x} \in \Omega$, compute ϕ^{n+1}, the solution of (43) at $t = t^{n+1}$.

Remark 2. Observe that the problem (43) is nonlinear. For solving it, we have adopted a linear iterative approach. More precisely, at each Darcy-scale mesh point $\boldsymbol{x} \in \Omega$ and time t^n, with $L > 0$ large enough and letting $i \in \mathbb{N}$ be the iteration index,

17

assuming $\phi^{n+1,i-1}$ known and Y-periodic, one solves the system

$$
\begin{cases}
\nabla_{\boldsymbol{y}} \cdot (\boldsymbol{v}^n \phi^{n+1,i}) = \overline{A_\phi} \lambda \Delta_{\boldsymbol{y}} \psi^{n+1,i}, & \text{in } \mathcal{P}, \\[2mm]
\psi^{n+1,i} = \overline{A_\psi} \gamma(c^{n+1}) \left(\dfrac{\mathcal{C} P'(\phi^{n+1,i-1})}{\lambda} + \dfrac{I'(\phi^{n+1,i-1})}{\beta} \right. \\[3mm]
\qquad\qquad \left. + L(\phi^{n+1,i} - \phi^{n+1,i-1}) - \mathcal{C}\lambda \Delta_{\boldsymbol{y}} \phi^{n+1,i} \right), & \text{in } \mathcal{P}, \quad (49) \\[2mm]
\nabla_{\boldsymbol{y}} \phi^{n+1,i} \cdot \boldsymbol{n} = 0, \ \nabla_{\boldsymbol{y}} \psi^{n+1,i} \cdot \boldsymbol{n} = 0, & \text{on } \partial\mathcal{G}, \\[2mm]
\phi^{n+1,i} \text{ and } \psi^{n+1,i} \text{ are } Y\text{-periodic and } \dfrac{1}{\Phi} \displaystyle\int_{\mathcal{P}} \phi^{n+1,i} \, d\boldsymbol{y} = 2S^{n+1} - 1.
\end{cases}
$$

The velocity $\boldsymbol{v}^n$ is given in (44), computed for $t = t^n$. As a starting guess we choose the phase field at the previous time, $\phi^{n+1,0} = \phi^n$. However, the numerical experiments showed that the iterations are convergent regardless of the initial guess.
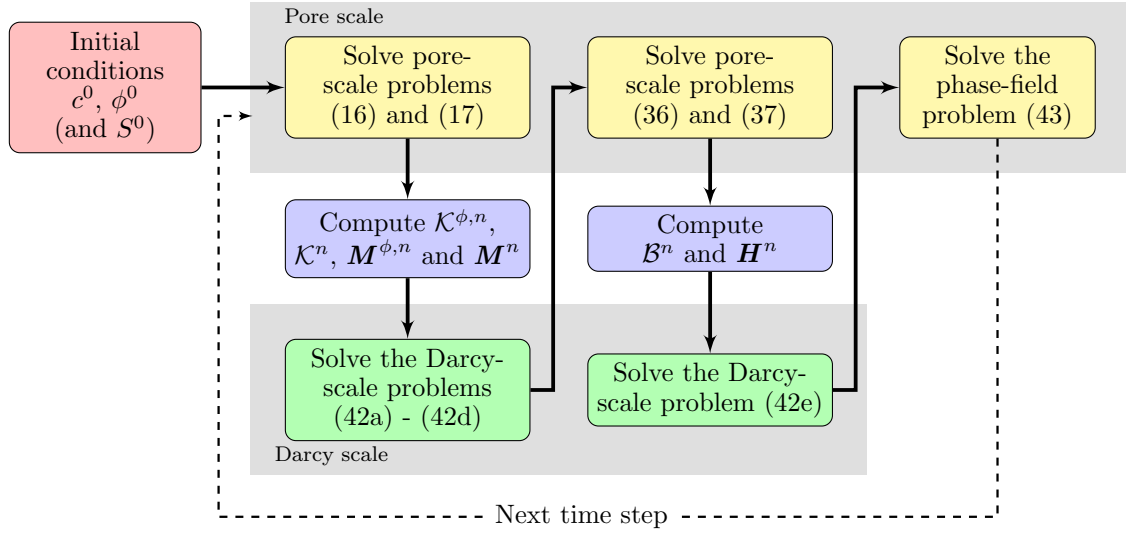
Figure 2. The two-scale scheme.

The two-scale scheme is presented in Figure 2. Observe that the time stepping in (47) is explicit. For the spatial discretization, we consider $\mathfrak{T}_H$, a Darcy-scale triangular partition of the domain Ω. An element $T \in \mathfrak{T}_H$ has diameter H_T. For each Darcy-scale element T, the effective quantities are computed by solving the cell problems defined in a pore-scale domain $\mathcal{P}$. The triangular partition $\mathfrak{T}_h$ of $\mathcal{P}$ consists of elements T_μ of diameter h_{T_μ}. We let $H := \max\limits_{T \in \mathfrak{T}_H} H_T$ and $h := \max\limits_{T_\mu \in \mathfrak{T}_h} h_{T_\mu}$. The numerical solutions of the pore- and Darcy-scale problems (17), (37), (43), (46) and (48) are computed using the lowest order Raviart-Thomas elements (see [47]). For the pore-scale problems (16) and (36) we use the Crouzeix–Raviart elements (see [48, Section 8.6.2]).

To compute the evolution of the phase field accurately and, implicitly, of the effective parameters, one needs a fine pore-scale mesh for each cell problem. This mesh needs to be fine enough to resolve the diffuse interface zone of the phase-field. More details on the mesh construction can be found in [49–51].

18

5. Numerical results

In this section, we present two numerical experiments, carried out in the 2D case. We consider the (Darcy-scale) domain $\Omega = (0, 1) \times (0, \frac{1}{2})$ and take T = 1 as final time. In both tests, a zero initial concentration is considered, $c^0 \equiv 0$, while the initial phase field ϕ^0 does not change with the vertical Darcy-scale variable x_2 (see below). Therefore, the saturation S^0, obtained from (26), depends only on the horizontal variable, $S^0(\boldsymbol{x}) = f(x_1)$. The function f is within the range $[0.66, 0.86]$ (see Figure 3).

Every pore-scale domain Y has a centered inner grain $\mathcal{G} = (0.4, 0.6) \times (0.4, 0.6)$. This gives a constant porosity, $\Phi = 0.96$. For each $\boldsymbol{x} \in \Omega$, the initial phase field $\phi^0(\boldsymbol{x}, \cdot)$ is radially symmetric up to not being defined on $\mathcal{G}$. Its value changes from -1 (fluid 2, around $\mathcal{G}$) to 1 (fluid 1, the outer part of $\mathcal{P}$) in a thin, diffuse region around a circle. The radius of it changes in the x_1-direction but not in the x_2-direction.

Homogeneous Neumann boundary conditions are imposed for c and p at the upper and lower boundaries of Ω. The same applies for c at the right boundary. The pressure and concentration are prescribed at the left boundary, $p = p_{in} = 2$ and $c = c_{in}$. In the two tests, the only varying data is c_{in}. At the right boundary, a lower pressure is imposed, $p = p_{out} = 0$, causing a horizontal flow to the right. Therefore, the left and right boundaries are called in- and outflow boundaries. This is sketched in Figure 3.
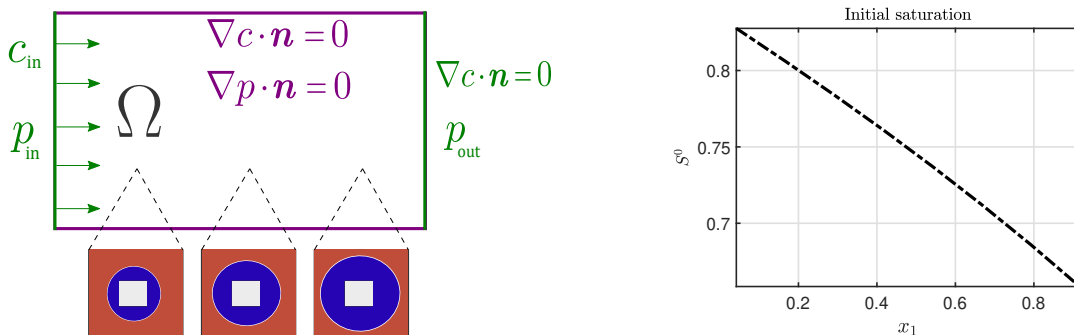
Figure 3. A sketch of the Darcy-scale boundary conditions and of the initial phase field at various locations (left), and the corresponding initial saturation (right).

We use the following non-dimensional parameters

$$\lambda = 0.02, \quad \mu_1 = 1, \quad \mu_2 = 0.9, \quad \beta = \overline{\mathrm{Ca}} = \overline{\mathrm{Eu}} = \overline{\mathrm{Re}} = \overline{\mathrm{Pe}_c} = \overline{\mathrm{A}_\phi} = \overline{\mathrm{A}_\psi} = 1,$$

and the given constant $\mathcal{C} = \frac{3}{2\sqrt{2}}$. To illustrate the effect of the solute-dependent surface tension, we let $\gamma(c) = -(100c + 1)$, and consider the following situations.

Test case 1. First we let $c = c_{in} = 0$. Then, the concentration remains 0 during the whole simulation.

Test case 2. With $c = c_{in} = 1$, the concentration is increasing in time for every $\boldsymbol{x}$, but remains decreasing in the x_1-direction for any t.

For the numerical simulation we use $\Delta t = 0.04$, thus carry out 25 time steps. For the spatial discretization we construct a uniform Darcy-scale (coarse) mesh with mesh diameter $H = 0.1767$. At the pore scale we consider a uniform (fine) mesh with mesh diameter $h = 0.0283$.

In both test cases, the Darcy-scale solution components do not change with the vertical variable x_2. Therefore, these solutions are presented as a 1D projection/cut

in the x_1-direction. Also, to illustrate the evolution in time of various Darcy-scale quantities, we choose $\boldsymbol{x}_{\text{ref}} = (0.9167, 0.2917)$ as a reference Darcy-scale point. The behaviour in other points is similar. Also, to compare the results obtained in the two test cases, we present the evolution in time of the difference in the variables, calculated at $\boldsymbol{x}_{\text{ref}}$. E.g. for the saturation S we compute

$$\delta S(t, \boldsymbol{x}_{\text{ref}}) := S(t, \boldsymbol{x}_{\text{ref}})\big|_{(\text{TestCase2})} - S(t, \boldsymbol{x}_{\text{ref}})\big|_{(\text{TestCase1})},$$

for $t \in [0, 1]$, and similarly for other Darcy-scale variables, or effective matrix components and vector elements.
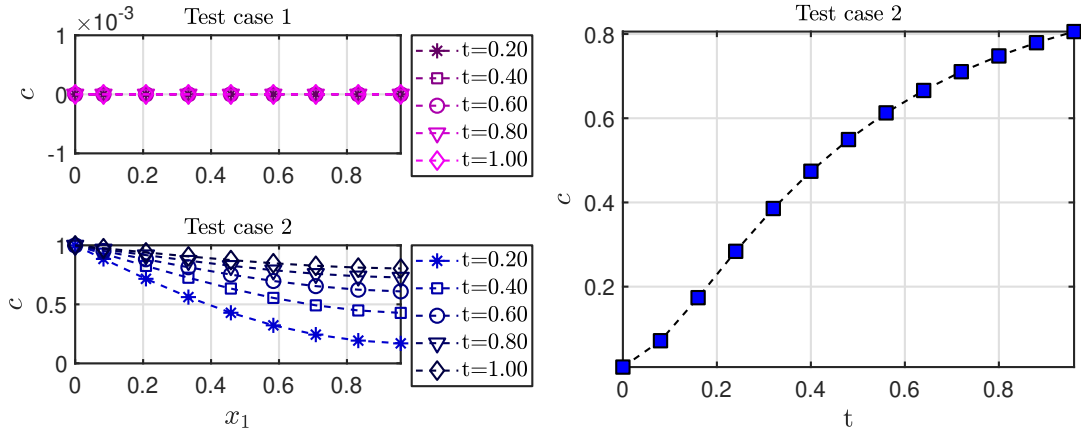
Figure 4. The concentration $c(t, \cdot)$ at five time steps for test case 1 (left-top) and test case 2 (left-bottom). The evolution of $c(\cdot, \boldsymbol{x}_{\text{ref}})$ for test case 2 (right).

The left plots in Figure 4 present the numerical approximation of the concentration c for the two test cases. Observe that, as expected, c remains 0 everywhere in the first test case. The right plot in Figure 4 shows the evolution of the concentration at the Darcy-scale reference point $\boldsymbol{x}_{\text{ref}}$ for the second test case.
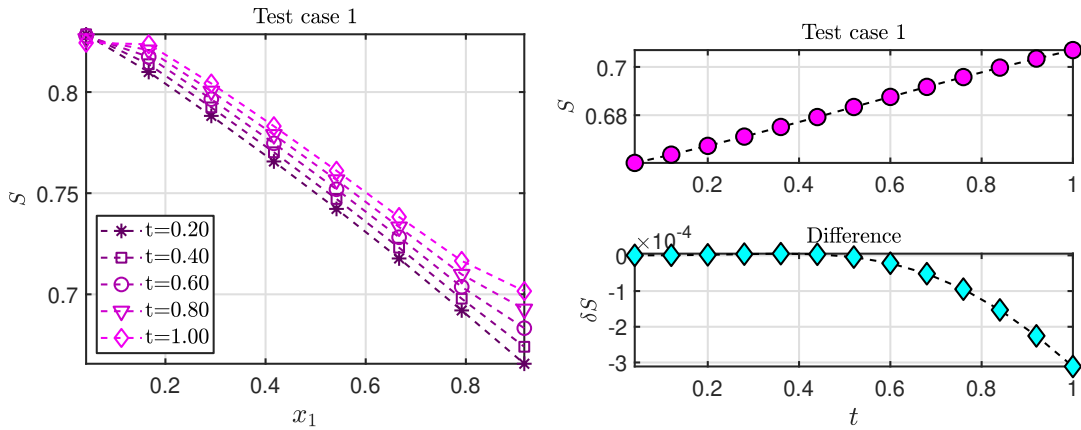
Figure 5. The saturation $S(t, \cdot)$ at five time steps, for the test case 1 (left). The evolution of $S(\cdot, \boldsymbol{x}_{\text{ref}})$ for the test case 1 (right-top) and of the difference $\delta S(\cdot, \boldsymbol{x}_{\text{ref}})$ between the two test cases (right-bottom).

The left plot in Figure 5 shows the numerical approximation of the saturation S

20

for the test case 1. The saturation increases with time, but remains decreasing in the x_1-direction. The evolution in time of $S(\cdot, \boldsymbol{x}_{\text{ref}})$ is presented in the upper right plot. The lower right plot shows the difference in the saturations between the two test cases. Note that the saturation S is lower in the second test case as it increases less with time compared to the first test case. This is indirectly caused by the difference in the surface tension, leading to, as we will see below, a difference in the ϕ-weighted Darcy-scale velocity $\bar{\boldsymbol{v}}^{\phi}$.
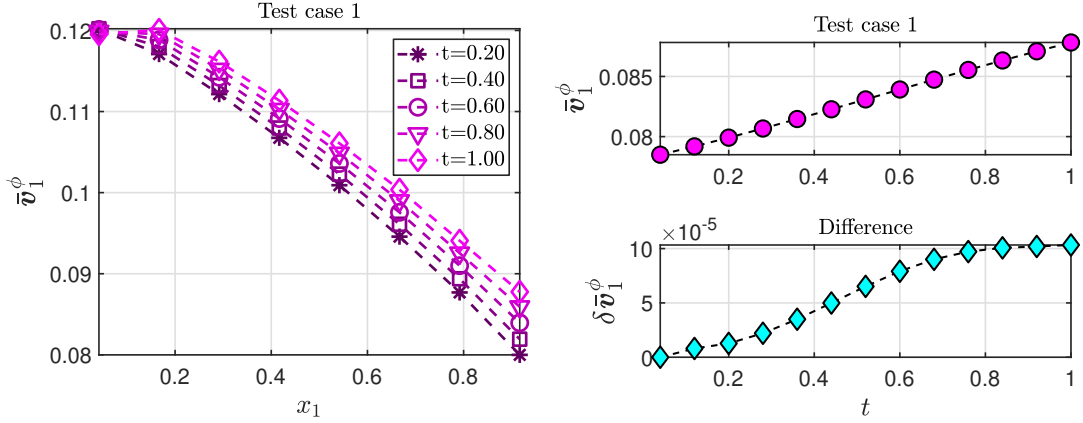
Figure 6. The horizontal component of the (Darcy-scale) velocity $\bar{\boldsymbol{v}}^{\phi}(t, \cdot)$, computed at five time steps, for the test case 1 (left). The evolution of $\bar{v}_1^{\phi}(\cdot, \boldsymbol{x}_{\text{ref}})$ for the test case 1 (right-top) and of the difference $\delta \bar{v}_1^{\phi}(\cdot, \boldsymbol{x}_{\text{ref}})$ between the two test cases (right-bottom).

Due to the setup, the horizontal component of the Darcy-scale velocity $\bar{\boldsymbol{v}}$ will remain constant over the domain. However, the velocity $\bar{\boldsymbol{v}}^{\phi}$ can still vary, and, as follows from (42c), this causes changes in the saturation. Moreover, this change becomes more natural when considering (45), in which the phase velocity is depends on the (here, constant) $\bar{\boldsymbol{v}}$ and the variable $\bar{\boldsymbol{v}}^{\phi}$. We note that the vertical component of $\bar{\boldsymbol{v}}^{\phi}$ is zero, hence only the horizontal component is shown in Figure 6. As we see from the left plot in Figure 6, the horizontal component has a negative derivative with respect to x_1 throughout the domain, yielding an increasing saturation. However, from the difference shown in the lower right plot of Figure 6, the horizontal component of $\bar{\boldsymbol{v}}^{\phi}$ is higher in the test case 2 than in the test case 1. Hence, its derivative, though negative, is closer to 0, yielding a smaller increase in the saturation. Note that the reference point $\boldsymbol{x}_{\text{ref}}$ is at the right part of the domain, and that saturation and velocity changes in points further left are less than in $\boldsymbol{x}_{\text{ref}}$.
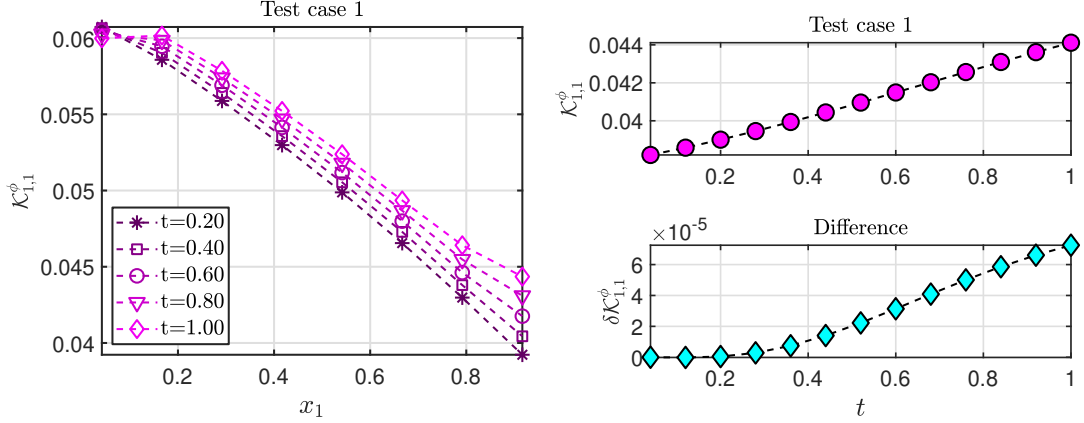
Figure 7. The first component of $\mathcal{K}^\phi(t, \cdot)$, computed at five time steps, for test case 1 (left). The evolution of $\mathcal{K}^\phi_{1,1}(\cdot, \boldsymbol{x}_{\text{ref}})$ for the test case 1 (right-top) and of the difference $\delta\mathcal{K}^\phi_{1,1}(\cdot, \boldsymbol{x}_{\text{ref}})$ between the two test cases, at $\boldsymbol{x}_{\text{ref}}$ (right-bottom).

Figure 7 and Figure 8 are displaying the evolution of the effective parameters from (42d), which are influencing $\bar{\boldsymbol{v}}^\phi_1$. The left plot in Figure 7 displays $\mathcal{K}^\phi_{1,1}$, while the time evolution of $\boldsymbol{M}^\phi_1$ is shown in Figure 8. Comparing the sizes, and accounting for the fact that the horizontal pressure drop is around -2, and $\gamma(c)$ is in the range $[-101, -1]$, it becomes clear that the horizontal pressure drop and the evolution of $\mathcal{K}^\phi_{1,1}$ dominate the changes in $\bar{\boldsymbol{v}}^\phi_1$ in both test cases considered here. Observe that, similarly to $\bar{\boldsymbol{v}}^\phi_1$, $\mathcal{K}^\phi_{1,1}$ increases with time in the right part of the domain, and stronger for the test case 2, causing a decreased divergence of $\bar{\boldsymbol{v}}^\phi$.
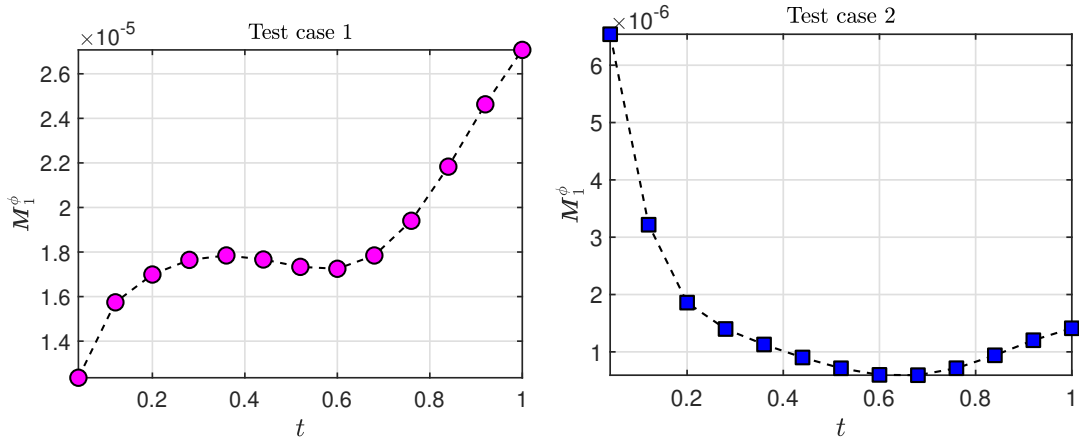
Figure 8. The evolution of the first element of $\boldsymbol{M}^\phi(\cdot, \boldsymbol{x}_{\text{ref}})$ for the two test cases.

22
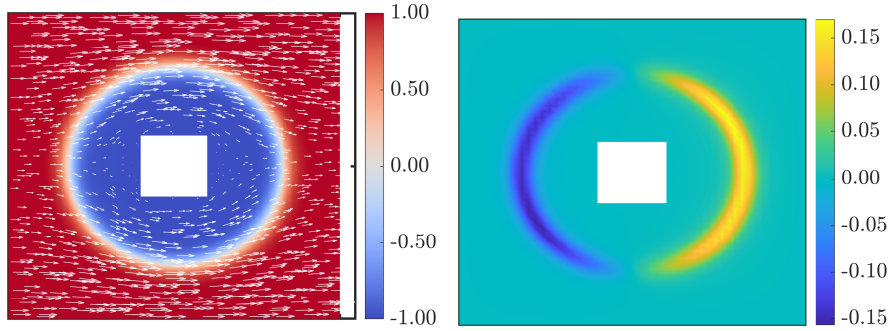
Figure 9. The evolution of the pore-scale phase field in the test case 1 (left) and the difference of the phase field $\delta\phi$ between the two test cases (right) corresponding to the Darcy-scale location $\boldsymbol{x}_{\mathrm{ref}}$ at time $t = 1$.

The changes of $\mathcal{K}^\phi$ is depending on how the pore-scale phase-field evolves, which again depends on the surface tension. In Figure 9 we display the pore-scale phase field obtained at the final time $t = 1$, at the reference point $\boldsymbol{x}_{\mathrm{ref}}$. The left plot in Figure 9 shows the numerical approximation of the phase field $\phi(1, \boldsymbol{x}_{\mathrm{ref}}, \boldsymbol{y})$ and the pore-scale velocity $\boldsymbol{v}(1, \boldsymbol{x}_{\mathrm{ref}}, \boldsymbol{y})$ (with $\boldsymbol{y} \in \mathcal{P}$), obtained in the first test case. Note that the pore-scale flow field is oriented mainly towards right. This immediately implies that the Darcy-scale velocity $\bar{\boldsymbol{v}}$ has the same orientation. The difference in the phase fields between the two test cases is displayed in the right plot. This difference is calculated for $t = 1$ and at $\boldsymbol{x}_{\mathrm{ref}}$, using

$$\delta\phi(1, \boldsymbol{x}_{\mathrm{ref}}, \boldsymbol{y}) = \phi(1, \boldsymbol{x}_{\mathrm{ref}}, \boldsymbol{y})\big|_{(\mathrm{TestCase2})} - \phi(1, \boldsymbol{x}_{\mathrm{ref}}, \boldsymbol{y})\big|_{(\mathrm{TestCase1})}.$$

As follows from the right plot, the phase-field profile in the second case corresponds to fluid 2 being shifted slightly to the left compared to the test case 1.

6. Conclusion

We have derived a two-scale model for the two-phase flow in a porous medium. The model takes into account the variations in the surface tension, caused by a surfactant soluble in one fluid phase. The starting point is the pore-scale model proposed in [30]. This is a Navier-Stokes-Cahn-Hilliard model for the flow, coupled with an advection-diffusion equation for solute concentration. In this way, the free boundaries separating the two fluid phases at the pore scale are approximated by thin diffuse interface regions, which allows formulating the problem in a fixed domain.

Using formal homogenization methods, we have derived a two-scale model consisting of mass conservation laws for the two phases and for the solute concentration, and of Darcy-type laws for the effective velocities. The latter include terms accounting for the concentration-dependent surface tension. These Darcy-scale laws involve effective parameters, which are obtained by solving local cell problems. These cell problems depend on the evolution of the phase field at the pore scale.

We have proposed a numerical algorithm building on the Euler explicit time discretization and on the lowest order Raviart-Thomas approximation in space. The explicit scheme requires solving seven pore-scale cell problems, defined for each Darcy-scale point. These cell problems depend on Darcy-scale variables concentration, pressure and saturation. At the same time, for solving the Darcy-scale equations, one

23

requires accurate calculations of the effective parameters, based on pore-scale quantities. These cell problems are generally small and parallelizable, allowing for efficient numerical strategies. In particular, for the phase-field cell problem, which is nonlinear and elliptic, we propose a simple, linear iterative scheme having a robust convergence, regardless of the initial guess.

Two test cases are presented, where the surface tension either remains constant, or where the changes in the concentration induce a varying surface tension. The fluids have different viscosities, but the viscosity ratio is small. The profiles of the Darcy-scale quantities display a similar behaviour in time and space in both test cases. Though small, differences in the results can be observed. In particular, the surfactant leads to decreased values of the saturation, as it affects the effective quantities, which depend on the pore-scale phase-field distribution.

Open issues are related to mesh refinement strategies at both the pore scale and the Darcy scale, as mentioned in [51]. Furthermore, adaptive strategies allowing to identify Darcy-scale points where the effective parameters need to be recalculated, and those where these values can be copied from points with a similar behaviour, could also improve the efficiency of the algorithm. Finally, implicit or semi-implicit higher-order numerical schemes for the two-scale model derived here need to be developed, as well as the rigorous analysis of the model and of the numerical approximation.

Disclosure statement

No potential conflict of interest was reported by the authors.

References

[1] Landa-Marban D, Radu FA, Nordbotten JM. Modeling and simulation of microbial enhanced oil recovery including interfacial area. Transp Porous Media. 2017;120(2):395–413.
[2] Wu Z, Yue X, Cheng T, et al. Effect of viscosity and interfacial tension of surfactant–polymer flooding on oil recovery in high-temperature and high-salinity reservoirs. J Petrol Explor Prod Technol. 2014;4(1):9–16.
[3] Mulligan MK, Rothstein JP. The effect of confinement-induced shear on drop deformation and breakup in microfluidic extensional flows. Phys Fluids. 2011;23(2):022004.
[4] Kovalchuk NM, Simmons MJ. Effect of surfactant dynamics on flow patterns inside drops moving in rectangular microfluidic channels. J Colloid Interface Sci. 2021;5(3):40.

[5] Craster RV, Matar OK. Dynamics and stability of thin liquid films. Rev Modern Phys. 2009;81(3):1131.

[6] Hartnett C, Seric I, Mahady K, et al. Exploiting the marangoni effect to initiate instabilities and direct the assembly of liquid metal filaments. Langmuir. 2017;33(33):8123–8128.

[7] Mikelić A, Paoli L. On the derivation of the buckley—leverett model from the two fluid navier—stokes equations in a thin domain. Comput Geosci. 1997;1(1):59–83.

[8] Sharmin S, Bringedal C, Pop IS. On upscaling pore-scale models for two-phase flow with evolving interfaces. Adv in Water Res. 2020;142:103646.

[9] Mikelić A. On an averaged model for the 2-fluid immiscible flow with surface tension in a thin cylindrical tube. Comput Geosci. 2003;7(3):183–196.

[10] Lunowa SB, Bringedal C, Pop IS. On an averaged model for immiscible two-phase flow with surface tension and dynamic contact angle in a thin strip. Stud Appl Math. 2021; 1:43.

[11] Fasano A, Mikelić A. The 3D flow of a liquid through a porous medium with absorbing and swelling granules. Interfaces Free Bound. 2002;4(3):239–261.

[12] Sweijen T, van Duijn CJ, Hassanizadeh SM. A model for diffusion of water into a swelling particle with a free boundary: Application to a super absorbent polymer. Chem Eng Sci. 2017;172:407–413.

[13] van Noorden TL. Crystal precipitation and dissolution in a porous medium: effective equations and numerical experiments. Multiscale Model Simul. 2008;7(3):1220–1236.

[14] Bringedal C, Berre I, Pop IS, et al. Upscaling of non-isothermal reactive porous media flow with changing porosity. Transp Porous Media. 2016;114(2):371–393.

[15] Bringedal C, Kumar K. Effective behavior near clogging in upscaled equations for non-isothermal reactive porous media flow. Transp Porous Media. 2017;120(3):553–577.

[16] Gaerttner S, Frolkovic P, Knabner P, et al. Efficiency and accuracy of micro-macro models for mineral dissolution. Water Resour Res. 2020 AUG;56(8).

[17] Caginalp G, Fife PC. Dynamics of layered interfaces arising from phase boundaries. SIAM J Appl Math. 1988;48(3):506–518.

[18] Li X, Lowengrub J, Rätz A, et al. Solving PDEs in complex geometries: a diffuse domain approach. Commun Math Sci. 2009;7(1):81–107.

[19] Boyer F, Lapuerta C, Minjeaud S, et al. Cahn-Hilliard/Navier-Stokes model for the simulation of three-phase flows. Transp Porous Media. 2010;82(3):463–483.

[20] Kim J. Phase-field models for multi-component fluid flows. Commun Comput Phys. 2012; 12(3):613–661.

[21] van Noorden TL, Eck C. Phase field approximation of a kinetic moving-boundary problem modelling dissolution and precipitation. Interfaces Free Bound. 2011;13(1):29–55.

[22] Bringedal C, Von Wolff L, Pop IS. Phase field modeling of precipitation and dissolution processes in porous media: upscaling and numerical experiments. Multiscale Model Simul. 2020;18(2):1076–1112.

[23] Redeker M, Rohde C, Pop IS. Upscaling of a tri-phase phase-field model for precipitation in porous media. IMA J Appl Math. 2016;81(5):898–939.

[24] Rohde C, von Wolff L. Homogenization of Nonlocal Navier–Stokes–Korteweg Equations for Compressible Liquid-Vapor Flow in Porous Media. SIAM J Math Anal. 2020; 52(6):6155–6179.

[25] Guo Z, Lin P. A thermodynamically consistent phase-field model for two-phase flows with thermocapillary effects. Journal of Fluid Mechanics. 2015;766:226–271.

[26] Mikelić A, Wheeler MF, Wick T. Phase-field modeling of a fluid-driven fracture in a poroelastic medium. Comput Geosci. 2015;19(6):1171–1195.

[27] Lee S, Mikelić A, Wheeler MF, et al. Phase-field modeling of two phase fluid filled fractures in a poroelastic medium. Multiscale Model Simul. 2018;16(4):1542–1580.

[28] Cahn JW, Hilliard JE. Free energy of a nonuniform system. i. interfacial free energy. J Chem Phys. 1958;28(2):258–267.

[29] Abels H, Garcke H, Grün G. Thermodynamically consistent, frame indifferent diffuse interface models for incompressible two-phase flows with different densities. Math Models

Methods App Sci. 2012;22(03):1150013, 40.

[30] Garcke H, Lam KF, Stinner B. Diffuse interface modelling of soluble surfactants in two-phase flow. Commun Math Sci. 2014;12(8):1475–1522.

[31] Chen J, Sun S, Wang X. Homogenization of two-phase fluid flow in porous media via volume averaging. J Comput Appl Math. 2019;353:265–282.

[32] Schmuck M, Pradas M, Pavliotis GA, et al. Derivation of effective macroscopic Stokes-Cahn-Hilliard equations for periodic immiscible flows in porous media. Nonlinearity. 2013; 26(12):3259–3277.

[33] Daly KR, Roose T. Homogenization of two fluid flow in porous media. Proc A. 2015; 471(2176):20140564, 20.

[34] Baňas v, Mahato HS. Homogenization of evolutionary Stokes-Cahn-Hilliard equations for two-phase porous media flow. Asymptot Anal. 2017;105(1-2):77–95.

[35] Zhu G, Li A. Interfacial dynamics with soluble surfactants: A phase-field two-phase flow model with variable densities. Adv Geo-Energy Res. 2020;4(1):86–98.

[36] Frank F, Liu C, Alpak FO, et al. A finite volume / discontinuous galerkin method for the advective cahn–hilliard equation with degenerate mobility on porous domains stemming from micro-ct imaging. Comput Geosci. 2018;22(2):543–563.

[37] Ray D, Liu C, Riviere B. A discontinuous galerkin method for a diffuse-interface model of immiscible two-phase flows with soluble surfactant. Comput Geosci. 2021;25(5):1775–1793.

[38] Picchi D, Battiato I. The impact of pore-scale flow regimes on upscaling of immiscibletwo-phase flow in porous media. Water Resour Res. 2018;54(9):6683–6707.

[39] Quintard M, Whitaker S. Transport in ordered and disordered porous media: volume-averaged equations, closure problems, and comparison with experiment. Chem Eng Sci. 1993;48(14):2537–2564.

[40] Lasseux D, Ahmadi A, Arani AAA. Two-phase inertial flow in homogeneous porous media: A theoretical derivation of a macroscopic model. Transp Porous Media. 2008;75(3):371–400.

[41] Mikelić A. A convergence theorem for homogenization of two-phase miscible flow through fractured reservoirs with uniform fracture distributions. Appl Anal. 1989;33(3-4):203–214.

[42] Bourgeat A, Luckhaus S, Mikelić A. Convergence of the homogenization process for a double-porosity model of immiscible two-phase flow. SIAM J Math Anal. 1996;27(6):1520–1543.

[43] Amaziane B, Jurak M, Vrbaški A. Homogenization results for a coupled system modelling immiscible compressible two-phase flow in porous media by the concept of global pressure. Appl Anal. 2013;92(7):1417–1433.

[44] Bunoiu R, Cardone G, Kengne R, et al. Homogenization of 2D Cahn-Hilliard-Navier-Stokes system. J Elliptic Parabol Equ. 2020;6(1):377–408.

[45] Metzger S, Knabner P. Homogenization of two-phase flow in porous media from pore to Darcy scale: a phase-field approach. Multiscale Model Simul. 2021;19(1):320–343.

[46] Kim J. A continuous surface tension force formulation for diffuse-interface models. J Comput Phys. 2005;204(2):784–804.

[47] Bahriawati C, Carstensen C. Three MATLAB implementations of the lowest-order Raviart-Thomas MFEM with a posteriori error control. Comput Methods Appl Math. 2005;5(4):333–361.

[48] Boffi D, Brezzi F, Fortin M. Mixed finite element methods and applications. Vol. 44. Springer; 2013.

[49] Bastidas M, Bringedal C, Pop IS. A two-scale iterative scheme for a phase-field model for precipitation and dissolution in porous media. Appl Math Comput. 2021;396:125933.

[50] Bastidas M, Bringedal C, Pop IS, et al. Numerical homogenization of non-linear parabolic problems on adaptive meshes. J Comput Phys. 2020;425:109903.

[51] Bastidas M, Sharmin S, Bringedal C, et al. A numerical scheme for two-scale phase-field models in porous media. In: Conference Proceedings of the 6th ECCOMAS Young Investigators Conference YIC2021, Universitat Politècnica de València, Spain; 2021. (accepted).

▶▶ UHASSELT

UHasselt Computational Mathematics Preprint Series

2021

2020

UP-20-07 *M. Gahn, M. Neuss-Radu, I.S. Pop*, **Homogenization of a reaction-diffusion-advection problem in an evolving micro-domain and including nonlinear boundary conditions**, 2020

UP-20-06 *S.B. Lunowa, C. Bringedal, I.S. Pop*, **On an averaged model for immiscible two-phase flow with surface tension and dynamic contact angle in a thin strip**, 2020

UP-20-05 *M. Bastidas Olivares, C. Bringedal, I.S. Pop*, **An adaptive multi-scale iterative scheme for a phase-field model for precipitation and dissolution in porous media**, 2020

UP-20-04 *C. Cancès, J. Droniou, C. Guichard, G. Manzini, M. Bastidas Olivares, I.S. Pop*, **Error estimates for the gradient discretisation of degenerate parabolic equation of porous medium type**, 2020

UP-20-03 *S.B. Lunowa, I.S. Pop, and B. Koren*, **Linearization and Domain Decomposition Methods for Two-Phase Flow in Porous Media Involving Dynamic Capillarity and Hysteresis**, 2020

UP-20-02 *M. Bastidas, C. Bringedal, and I.S. Pop*, **Numerical simulation of a phase-field model for reactive transport in porous media**, 2020

UP-20-01 *S. Sharmin, C. Bringedal, and I.S. Pop*, **Upscaled models for two-phase flow in porous media with evolving interfaces at the pore scale**, 2020